



Vision and Rain

KSHITIZ GARG AND SHREE K. NAYAR

Department of Computer Science, Columbia University, New York, NY, 10027

kshitiz@cs.columbia.edu

nayar@cs.columbia.edu

Received April 17, 2006; Accepted December 18, 2006

First online version published in February, 2007

Abstract. The visual effects of rain are complex. Rain produces sharp intensity changes in images and videos that can severely impair the performance of outdoor vision systems. In this paper, we provide a comprehensive analysis of the visual effects of rain and the various factors that affect it. Based on this analysis, we develop efficient algorithms for handling rain in computer vision as well as for photorealistic rendering of rain in computer graphics. We first develop a photometric model that describes the intensities produced by individual rain streaks and a dynamic model that captures the spatio-temporal properties of rain. Together, these models describe the complete visual appearance of rain. Using these models, we develop a simple and effective post-processing algorithm for detection and removal of rain from videos. We show that our algorithm can distinguish rain from complex motion of scene objects and other time-varying textures. We then extend our analysis by studying how various factors such as camera parameters, rain properties and scene brightness affect the appearance of rain. We show that the unique physical properties of rain—its small size, high velocity and spatial distribution—makes its visibility depend strongly on camera parameters. This dependence is used to reduce the visibility of rain during image acquisition by judiciously selecting camera parameters. Conversely, camera parameters can also be chosen to enhance the visibility of rain. This ability can be used to develop an inexpensive and portable camera-based rain gauge that provides instantaneous rain-rate measurements. Finally, we develop a rain streak appearance model that accounts for the rapid shape distortions (i.e. oscillations) that a raindrop undergoes as it falls. We show that modeling these distortions allows us to faithfully render the complex intensity patterns that are visible in the case of raindrops that are close to the camera.

Keywords: physics-based vision, outdoor vision and weather, atmospheric scattering, appearance modeling, natural phenomena, video analysis, video enhancement

1. Vision Through Rain

Outdoor vision systems are used for various purposes such as surveillance and navigation. These systems use a variety of algorithms such as feature detection, stereo correspondence, tracking, segmentation, and object recognition. Each of these algorithms can be adversely affected by bad weather conditions. To make outdoor vision systems robust to different weather conditions we need to model their visual effects and develop algorithms to account for them.

Based on their physical properties and the type of visual effects they produce, weather conditions can be broadly classified into *steady* (fog, mist and haze) or

dynamic (rain, snow and hail). In the case of steady weather, constituent droplets are too small ($1\text{--}10\ \mu\text{m}$) to be individually detected by a camera. The intensity produced at a pixel is due to the aggregate effect of a large number of droplets within the pixel's solid angle (see Fig. 1(a)). Hence, volumetric scattering models such as attenuation and airlight (Middleton, 1952; McCartney, 1975) can be used to adequately describe the manifestations of steady weather. In the last few years, various algorithms (Narasimhan and Nayar, 2002, 2003; Schechner et al., 2001; Cozman and Krotkov, 1997; Oakley and Satherley, 1998; Tan and Oakley, 2000) have been developed for removing the effects of steady weather from images and for recovering the 3D structure (Narasimhan

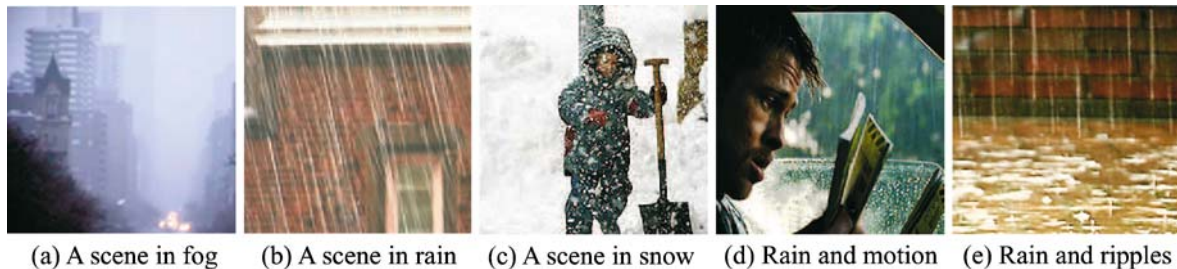


Figure 1. The visual appearances of steady (fog) and dynamic (rain) weather conditions are significantly different. (a) An image of a scene taken under foggy conditions. The intensity at each pixel is due to the aggregate effect of a large number of droplets within the pixel's field of view. An image of a scene taken in (b) rain and (c) snow. Individual motion-blurred raindrops and snowflakes are clearly visible. An algorithm that detects and removes rain must be robust to complex scene and camera motions as in (d) and at the same time insensitive to other time-varying textures such as the water ripples in (e).

and Nayar, 2002; Schechner et al., 2001; Cozman and Krotkov, 1997) of a scene.

In comparison, the effects of dynamic weather (rain and snow) are much more complex and have not been studied in detail. Rain and snow consists of particles that are 1000 times larger (0.1–10 mm) than those in steady weather. At such sizes, individual particles become visible to a camera. Figure 1(b) and (c) show motion-blurred images of rain and snow. The aggregate models used for steady weather are not applicable in these cases. Dynamic weather requires models that can describe the intensities produced by individual particles and also capture the spatial and temporal effects of a large number of particles moving at high speeds (as in rain) and with possibly complex trajectories (as in snow).

In this paper, we focus on rain, a common dynamic weather condition. We have two main goals: (a) To understand the complex visual appearance of rain and (b) to develop algorithms that make outdoor vision applications more robust to rain. The following are our main contributions:

Modeling the Appearance of Rain. We have developed a comprehensive model for the visual appearance of rain. Rain consists of large numbers of drops falling at high speeds. Each raindrop acts as a spherical lens that refracts and reflects light from a large field of view towards the camera, creating sharp intensity patterns in images. A group of such falling drops results in complex space and time-varying signals in images. In addition, due to the long exposure time of a camera, the intensities produced by rain are motion-blurred and hence depend on the background. We model these effects by developing separate photometric and dynamic models of rain. Together these models describe the complete visual appearance of rain.

Algorithm for Detection and Removal of Rain. Based on our appearance models, we have developed a simple algorithm for detection and removal of rain in videos. Our

algorithm uses the photometric and dynamic constraints derived from the appearance models to distinguish rain from other types of signals. This makes it effective in detecting and removing rain even in the presence of complex scene motions as in Fig. 1(d), and time-varying textures as in Fig. 1(e). Note that simple image processing techniques cannot distinguish rain from other types of signals and hence cannot be used for detection and removal of rain.

Analysis of Visibility of Rain. We extend our analysis of rain by studying how various factors, such as properties of rain, camera parameters, and scene brightness affect the appearance of rain in images and videos. Our analysis shows that the visibility of rain increases as the square of the raindrop size and decreases linearly with the brightness of the background scene. Most importantly, we show that the small size, high velocity and spatial distribution of raindrops make rain visibility dependent on camera parameters, such as exposure time and depth of field. We have conducted extensive experiments that verify our analytical models.

Rain Removal/Reduction Using Camera Parameters. Based on this analysis on visibility, we have developed a method that sets the camera parameters to remove/reduce the effects of rain without altering the appearance of the scene. This is possible because, given the finite resolution and sensitivity of the camera, a wide range of camera settings (exposure time, F-number, focus setting) produce essentially the same scene appearance. However, within this range the appearance of rain can vary significantly. Note that this approach does not require any post-processing and can be easily incorporated as a feature into consumer cameras. We present several experimental results that show our approach to be very effective in a wide range of scenarios. In the extreme cases of very heavy rain or fast moving objects that are close to the camera, our approach is not as effective. In such cases,

however, the post-processing algorithm discussed earlier can be used.

Camera Based Rain Gauge. Camera parameters can also be set to enhance the visual effects of rain. This can be used to build a camera-based rain gauge that measures rain rate. A major advantage of a camera-based rain gauge over a conventional one is that it can provide measurements on a much finer time scale. While specialized instruments such as the disdrometer (Schonhuber et al., 1994; Löffler-Mang and Joss, 2000) can also provide rain measurements at a fine time scale, they are very expensive and are not portable. In comparison, a vision-based rain gauge is cheap and portable.

Photorealistic Rendering of Rain Streaks Close to Camera. Raindrops undergo rapid shape distortions as they fall, often referred to as *oscillations*. The interaction of light with these oscillations produces a wide variety of complex brightness patterns within a rain streak. These patterns are particularly noticeable in close-up shots of rain, where raindrops project onto larger image streaks. We have developed a rain-streak appearance model that captures the complex interactions between the lighting direction, the viewing direction and the oscillation of a raindrop to render photorealistic rain streaks in images and videos. We have empirically verified our streak appearance model by comparing the rendered streaks with actual images of falling drops.

2. Previous Work

The effects of rain on vision systems have not been previously explored. However, rain has been extensively studied in the fields of atmospheric sciences, communications, architecture, and most recently, computer graphics. The goals of these fields are very different from those of vision. Here we briefly discuss some of the important work and aims of the different fields.

Atmospheric Sciences. Atmospheric sciences provide an extensive literature on the physical properties of rain such as raindrop size distribution (Marshall and Palmer, 1948), shape (Beard and Chuang, 1987; Tokay and Beard, 1996; Andsager et al., 1999) and velocity (Gunn and Kinzer, 1949). Studies also aim at designing novel instruments (Schonhuber et al., 1994; Löffler-Mang and Joss, 2000) and methods (Wang and Clifford, 1975; Bradley et al., 2000) to provide better measurement of the properties of rain and weather forecasting. Most of these studies, however, use active illumination (lasers and radars) and specialized detectors (photo-cells and radars) to measure or predict rain properties.

Communications. In communications, LIDAR and RADAR are commonly used to transmit signals. Rain attenuates the strength of the transmitted signal and introduces statistical noise, severely degrading the communication quality. Studies (Chu and Hogg, 1996; Borovoy et al., 1975; Deepak and Box, 1978) in the field have looked at various factors that can improve the quality of communication in rain such as the frequency of the transmission signal, the design of transmitter-detector system, and encoding schemes.

Architecture. In architecture, researchers have investigated the wetting and drying of facades (Flori, 1990) and weathering of buildings (Mulvin and Lewis, 1994) due to driving rain (rain that strikes buildings due to strong winds). The literature also provides a detailed analysis of the effects of wind on rain (Choi, 1995). The change in appearance of buildings due to rain and water has also been studied in computer graphics (Dorsey et al., 1996).

Computer Graphics. In graphics the goal is to generate visually realistic rain. Several methods for rendering rain have been developed in computer graphics, some of which are available in commercial softwares (Maya and Studio-Max). Recently, more computationally efficient algorithms (Starik and Werman, 2003; Wang and Wade, 2004; Langer et al., 2004) have been developed as well. All these methods, however, use very simple photometric models to render the appearance of rain streaks themselves. Most often streaks are approximated as rectangles or ellipses of constant brightness. Such simple photometric models can only be used when the rendered rain is at a great distance from the camera, in which case, all the streaks are thin enough to make the details of their brightness patterns irrelevant. For close-up shots of rain, each drop projects to a large image region, revealing the complex intensity pattern within it. For rendering such close-by streaks procedural textures have been used as in the movie “The Matrix Revolutions” Lomas (2005). This technique requires manually adjusting the texture parameters to match the appearance of real streaks, making it harder to use this approach for rendering the wide variation in streak appearance that arises due to lighting and view changes. We have developed a physics-based appearance model for photorealistic rendering of rain streaks including the variation due to lighting and viewing direction.

3. Physical Properties of Raindrops

Here we briefly summarize the physical properties of rain and make observations that are relevant to our goal of modeling the appearance of rain.

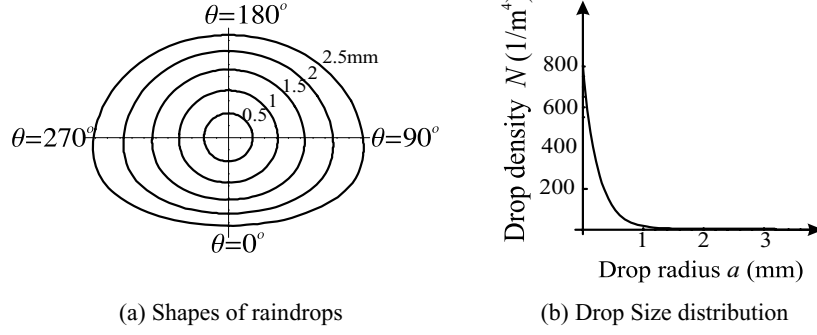


Figure 2. (a) The shapes of raindrops of various sizes (0.5–2.5 mm). The bases of the drops are flattened in the direction of fall ($\theta = 0$), mainly due to air pressure. Large drops are severely distorted, while smaller drops are almost spherical. (b) Marshall-Palmer drop size distribution: The number density of a raindrop as a function of drop size (for rainfall rate of 30 mm/hr). The density of drops decreases exponentially with size.

Shape of a Raindrop. A raindrop undergoes rapid shape distortions as it falls, a phenomenon often referred to as oscillations. For most vision tasks the effects of oscillations are insignificant¹ and hence a raindrop can be assumed to have a fixed shape often referred to as an *equilibrium* shape. The equilibrium shape of a drop depends on its size. Smaller drops are generally spherical in shape. However, as the size of the drop increases, it tends towards an oblate spheroid shape. Beard and Chuang (1987) describe the shape of a raindrop as a 10th order cosine distortion of a sphere:

$$r(\theta) = a \left(1 + \sum_{n=1}^{10} c_n \cos(n\theta) \right), \quad (1)$$

where, a is the radius of the undistorted sphere, $c_1 \dots c_{10}$ are the coefficients that depend on the radius of the drop and θ is the polar angle of elevation. $\theta = 0$ corresponds to the direction of the fall. The shapes of the drops of various sizes (0.5 – 2.5 mm) are shown in Fig. 2(a).

Size of a Raindrop. Raindrops show a wide distribution of size. A commonly used empirical distribution for raindrop size is the Marshall-Palmer distribution (Marshall and Palmer, 1948) and is given by $N(a) = 8 \times 10^6 e^{-8200 \cdot h^{-0.21} a}$, where, h is the rain rate given in mm/hr, a is the radius of the drop in meters and $N(a)$ is the number of raindrops per unit volume that contains sizes within the interval $(a, a + da)$. Figure 2(b) shows the Marshall-Palmer distribution for a typical rainfall rate of 30 mm/hr. Note that the drops that make up a significant fraction of rain are less than 1 mm in size. As seen from Figure 2(a), the drops with radii less than 1 mm are not severely distorted and their shapes can be well approximated by a sphere. Therefore, we will model raindrops as transparent spheres of water.

Velocity of a Raindrop. As a raindrop falls, it attains a constant velocity, called the terminal velocity (Manning, 1993). Gunn and Kinzer (1949) present an empirical study of the terminal velocities of falling raindrops for different drop sizes. Their observations show that the terminal velocity \bar{v} of a raindrop of radius a can be expressed as a function of its size and is given by $\bar{v} = 200 \sqrt{a}$.

Spatial Distribution of Raindrops. The individual raindrops are distributed randomly in 3D volume. This distribution is usually assumed to be uniform (Manning, 1993; Wang and Clifford, 1975). Thus the probability density of finding an i th drop at the position \vec{r}_i in an arbitrary volume V is given by $p(\vec{r}_i) = 1/V$. Also the probability $P(k)$ that k number of drops exist in a volume V is given by a Poisson distribution (Manning, 1993), $P(k) = e^{-\bar{n}} (\bar{n})^k / k!$, where, $\bar{n} = \rho V$ is the mean number of drops and ρ is the density of rain. In addition, it can be assumed that the statistical properties of the distribution remains constant over small regions in space (meters) and short time intervals (minutes) which are typical in vision tasks. We will use these observations while deriving a model that captures the dynamics of rain.

4. Appearance Model for Rain

The visual appearance of rain consists of two main components as illustrated in Fig. 3: (1) the dynamics, that captures the spatio-temporal correlation produced by projection of large numbers of falling drops onto the image plane (see Fig. 3(a)) and (2) the photometry, that is, the intensities produced by individual raindrops. To model photometry we study the appearance of transparent “stationary” raindrops (without motion-blur) as in Fig. 3(b). We then model the intensities of motion-blurred rain streaks that arise due to finite integration of a camera (see Fig. 3(c)). These dynamic and photometric models together describe the complete visual

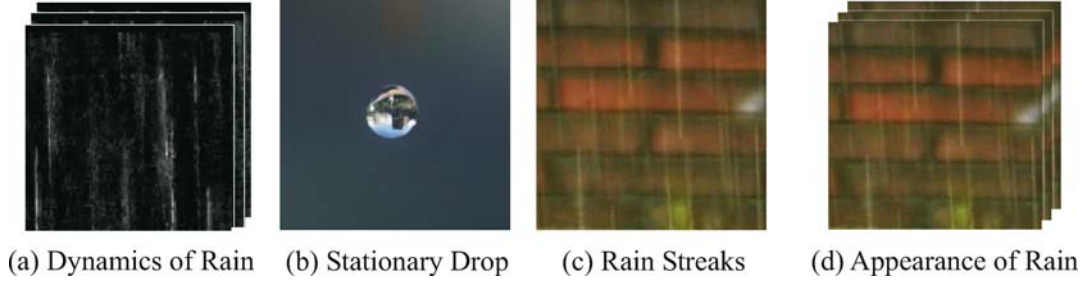


Figure 3. Visual appearance of rain. (a) Dynamics of rain. Signal produced by projection of fast moving drops on the imaging plane. (b–c) Photometry of a raindrop. (b) Appearance of a stationary raindrop. Note that appearance of a stationary raindrop depends on the environmental illumination it refracts and reflects towards the camera. (c) Motion-blurred intensities of rain streaks. Falling raindrops produce motion-blurred intensities that depend on the background. (d) Appearance of rain. The effects produced by rain on an imaging system are a combination of the dynamics of rain and its photometry.

appearance of rain. We now describe each of these in detail.

4.1. Dynamics of Rain

Consider a camera observing a volume of rain. Drops are randomly distributed in this volume and fall with high velocities. The projection of these drops onto the image plane produces a time-varying random field in image space which represents the dynamics of rain. For now, we consider only the image projections of the drops and not their intensities. Thus, the dynamics of rain may be represented by a binary field

$$b(\vec{r}, t) = \begin{cases} 1, & \text{if drop projects to location } \vec{r} \text{ at time } t; \\ 0, & \text{otherwise,} \end{cases} \quad (2)$$

where \vec{r} represents the spatial coordinates in the image and t is time. Initially, we consider both the space and time parameters, \vec{r} and t , to be continuous.

As mentioned in Section 3, we assume that the distribution of drops in the volume is uniform over space and time. Under this condition, the binary random field $b(\vec{r}, t)$ is *wide sense stationary* in space and time (Manning, 1993). This implies that the correlation function $R_b(\vec{r}_1, t_1; \vec{r}_2, t_2)$ depends only on differences in the image coordinates ($\Delta\vec{r} = \vec{r}_1 - \vec{r}_2$) and the difference in time ($\Delta t = t_1 - t_2$). That is:

$$\begin{aligned} R_b(\vec{r}_1, t_1; \vec{r}_2, t_2) &\equiv \frac{1}{L} \int_0^L b(\vec{r}_1, t_1 + t) b(\vec{r}_2, t_2 + t) dt \\ &= R_b(\Delta\vec{r}, \Delta t), \end{aligned} \quad (3)$$

where, the correlation R_b is computed over a large time period $[0, L]$. $R_b(\Delta\vec{r}, \Delta t)$ can be computed by measuring the temporal correlation with time lag Δt between the values of the binary field at points \vec{r} and $\vec{r} + \Delta\vec{r}$.

An important constraint arises due to the straight line motion of the drops. Consider a drop that falls with image

velocity \vec{v}_i . After time Δt , the displacement of this drop is $\vec{v}_i \Delta t$. Hence, the binary field at time instants t and $t + \Delta t$ are related as $b(\vec{r} + \vec{v}_i \Delta t, t + \Delta t) = b(\vec{r}, t)$. As a result, the correlation $R_b(\vec{r}, t; \vec{r} + \vec{v}_i \Delta t, t + \Delta t)$ is high. From Eq. (3), we write

$$R_b(\vec{r}, t; \vec{r} + \vec{v}_i \Delta t, t + \Delta t) = R_b(\vec{v}_i \Delta t, \Delta t). \quad (4)$$

This implies that the value of the binary field b at any two image coordinates, separated by $\vec{v}_i \Delta t$ in space, are correlated with time lag Δt . This is illustrated in Fig. 4(a).

The above correlation is analyzed in continuous domain. However, imaging systems have a finite pixel size p and a finite integration time T . In a discrete domain, let us denote the correlation by $R_b(\vec{m}p, nT)$, where \vec{m} is the displacement in integer image coordinates and n is the time lag in number of frames. The discrete binary field at any frame is obtained by integrating the continuous binary field over the time duration T . Hence, computing the correlation $R_b(\vec{m}p, nT)$ is equivalent to computing

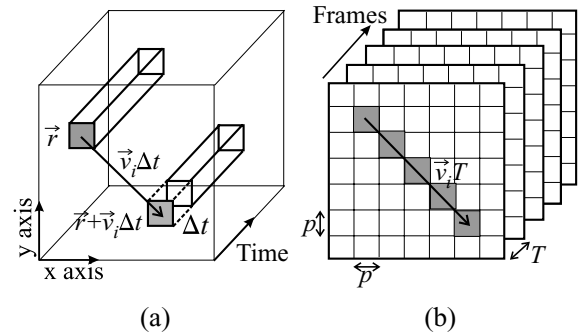


Figure 4. (a) Spatio-temporal correlation in a continuous space-time volume. Two image points \vec{r} and $\vec{r}_1 = \vec{r} + \vec{v}_i \Delta t$ are temporally correlated due to rain ($R_b(\vec{v}_i \Delta t, \Delta t)$ is high). (b) In a discrete domain, computing the correlation $R_b(\vec{m}p, 0)$ is equivalent to computing $R_b(\vec{v}_i \Delta t, \Delta t)$ over the entire duration $[0 \leq \Delta t \leq T]$. Hence, $R_b(\vec{m}p, 0)$ is high for pixels (shown shaded) separated by distance $[0 \leq \vec{m}p \leq \vec{v}_i T]$.

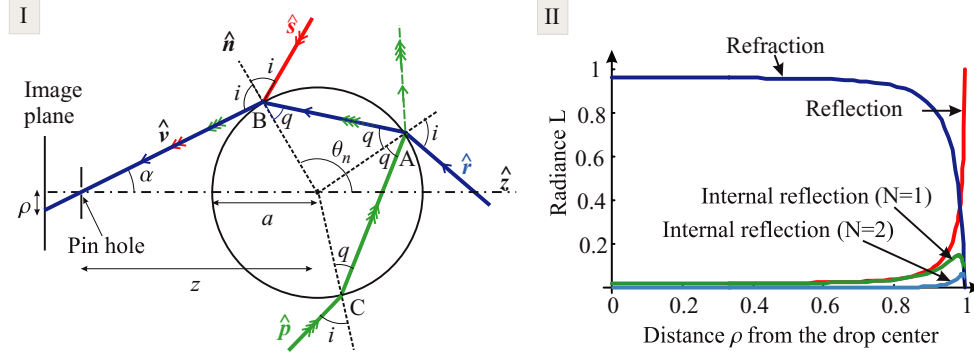


Figure 5. (a) Refraction, specular reflection and internal reflection by a raindrop. Light rays from directions \hat{r} , \hat{s} and \hat{p} reach the camera via refraction, specular reflection and internal reflection from the drop, respectively. Therefore, a drop's appearance is a complex mapping of the environmental radiance. (b) Drop radiance due to reflection, refraction and internal reflection plotted as a function of the distance ρ (see (a) and Eq. (6)). Here, $L_e = 1$. The radiance of the drop is mainly due to refraction. Specular and internal reflections are significant only at the periphery of the drop.

$R_b(\vec{v}_i \Delta t, \Delta t)$ over the entire time interval $[nT \leq \Delta t \leq (n+1)T]$. As a result, $R_b(\vec{m}p, nT)$ is high for all pixels separated by the distance $[\vec{v}_i nT \leq \vec{m}p \leq \vec{v}_i (n+1)T]$. Figure 4(b) shows the pixels for which the zeroth time lag correlation $R_b(\vec{m}p, 0)$ is high, where $[0 \leq \vec{m}p \leq \vec{v}_i T]$.

Note that different drops may have different (unknown) image velocity magnitudes $|\vec{v}_i|$ depending on their sizes and distances from the camera. However, within a local region, drops fall more or less in the same direction $\vec{v}_i/|\vec{v}_i|$. Hence, irrespective of the magnitude $|\vec{v}_i|$, the correlation R_b remains high in the direction $\vec{v}_i/|\vec{v}_i|$ of rain and low in all other directions. In summary, the binary field b produced by rain exhibits the following important properties:

- Since the distribution of drops is uniform over space and time, the binary field b due to rain is wide sense stationary.
- The temporal correlation between pixels in any neighborhood is high in the direction of rain and can be used to detect rain and compute its direction.

4.2. Photometry of a Raindrop

While modeling the dynamics we only considered the projection of the drops on the imaging plane. From this point onwards, we model the intensities produced by raindrops. We start by modeling the appearance of a stationary raindrop² (without motion-blur). We derive the appearance using simple geometric and photometric models of refraction and reflections (specular and internal) of environmental illumination from a raindrop.

4.2.1. Appearance of a Raindrop. As discussed in Section 3 the shape of a raindrop can be assumed to be spherical. Consider a point B on the surface of the raindrop with a surface normal \hat{n} as shown in Fig. 5. Scene

rays \hat{r} , \hat{s} and \hat{p} are directed towards the observer via refraction, specular reflection, and internal reflection respectively. Hence, the radiance $L(\hat{n})$ of point B is given by the sum of the radiance L_r of refracted ray, radiance L_s of specularly reflected ray and radiance L_p of internally reflected rays³, that is $L(\hat{n}) = L_r(\hat{n}) + L_s(\hat{n}) + L_p(\hat{n})$. Moreover, since these radiances depend on the environmental radiance L_e in the direction of the reflected or refracted ray, we can rewrite the above equation as

$$L(\hat{n}) = RL_e(\hat{r}) + SL_e(\hat{s}) + PL_e(\hat{p}), \quad (5)$$

where, R , S and P are the fraction of incident environmental radiance that reaches the camera after refraction, reflection and internal reflection, respectively. We refer to these fractions (R , S , P) as *radiance transfer functions*. In the following sections we derive exact expressions for these transfer functions and the geometric mapping from ray directions \hat{r} , \hat{s} and \hat{p} to the normal \hat{n} .

To derive the geometric mapping, we define a local coordinate frame placed at the center of the drop with its z -axis aligned with the optical axis of the camera. This choice of coordinate system is made to simplify the derivation of the mapping. When the drop lies elsewhere, the z -axis of the local coordinate frame can be aligned with the viewing direction that passes through the center of the drop.⁴ Also, since the drop size is very small compared to distance of the environment, all ray directions are defined with respect to the center of the drop coordinate frame. In our analysis, we use either vector or angle notations. That is, a direction \hat{a} may also be denoted as (θ_a, ϕ_a) , where θ_a is the polar angle and ϕ_a is the azimuthal angle. The image coordinates of the drop are parameterized as (ρ, ϕ) , where ρ is the distance of an image point from the center of the circular image of the drop (see Fig. 5). The coordinates (ρ, ϕ) are related

to $\hat{n} \equiv (\theta_n, \phi_n)$ as

$$\rho = (f/z), a \sin \theta_n, \quad \phi = \phi_n. \quad (6)$$

Here, f is the effective focal length of the camera and z is the distance of the drop from the camera.

Contribution of Refraction. We start by considering the appearance of drop only due to refraction. The direction of the scene ray $\hat{r} \equiv (\theta_r, \phi_r)$ that reaches the camera after refraction from the points (A and B) can be easily computed (see Appendix 10.1(a)) by using Snell's law to be:

$$\begin{aligned} \theta_r &= 2(\pi - \theta_n) + \alpha - 2\sin^{-1}((\sin(\theta_n - \alpha))/\mu) \\ \phi_r &= \pi + \phi_n. \end{aligned} \quad (7)$$

Here, α is the angle between the ray \hat{v} and the optical axis of the camera. The radiance of the refracted ray \hat{r} can be obtained by considering the change in radiance at refraction points A and B. Using radiance transfer properties it can be shown (see Appendix 10.1(c)) that the radiance L_A of the refracted ray at point A is related to the incident environmental radiance $L_e(\hat{r})$ as:

$$L_A = (1 - k(i, \mu))\mu^2 L_e(\hat{r}), \quad (8)$$

where, $i = (\pi - \theta_n + \alpha)$ is the incident angle, μ is the refractive index of the water and k is the Fresnel's reflectivity coefficient for unpolarized light.⁵ Similarly, the radiance $L_r(\hat{n})$ of the refracted ray at point B, where q is the angle the ray AB makes with the surface normal at B is given by⁶ $L_r(\hat{n}) = (1 - k(q, \frac{1}{\mu}))(\frac{1}{\mu})^2 L_A$. Substituting L_A and noting that $k(q, \frac{1}{\mu}) = k(i, \mu)$ we obtain the radiance $L_r(\hat{n})$ of refracted ray and the radiance transfer function R of refracted ray as,

$$L_r(\hat{n}) = (1 - k(i, \mu))^2 L_e(\hat{r}) \quad R = (1 - k(i, \mu))^2. \quad (9)$$

Contribution of Reflection. The reflected ray reaches the camera after a single reflection at point B (see Fig. 5). The direction $\hat{s} \equiv (\theta_s, \phi_s)$ of the specular reflection is therefore related to the surface normal $\hat{n} \equiv (\theta_n, \phi_n)$ as

$$\theta_s = 2\theta_n - \pi - \alpha, \quad \phi_s = \phi_n. \quad (10)$$

The radiance $L_s(\hat{n})$ of the specular ray \hat{s} changes only at point B and is given by

$$L_s(\hat{n}) = k(i, \mu)L_e(\hat{s}) \quad S = k(i, \mu) \quad (11)$$

Contribution of Internal Reflection. A ray can reach the camera after reflecting once or more number of times

from the inner surface of the drop. In Fig. 5 we see a scene ray $\hat{p} \equiv (\theta_p, \phi_p)$ reaching the observer after a single internal reflection⁷ from point A. The direction of \hat{p} can be simply computed using refraction and reflection relations at interface points. In Appendix 10.1(b), we derive the geometric mapping from θ_p to θ_n for the general case of a ray that reflects N times from the inner surface of the drop before exiting the drop:

$$\theta_p = 2(i - q) + N(\pi - 2q) - \alpha, \quad \phi_p = \pi - \phi_n, \quad (12)$$

where, $i = \pi - \theta_n + \alpha$ and $q = \sin^{-1}(\sin(i)/\mu)$. The radiance $L_e(\hat{p})$ of the ray \hat{p} changes N times due to reflection and twice due to refraction. Hence, radiance $L_p(\hat{n})$ of the internally reflected ray is

$$\begin{aligned} L_p(\hat{n}) &= R^N S L_e(\hat{p}) = k(i, \mu)^N (1 - k(i, \mu))^2 L_e(\hat{p}) \\ P &= k(i, \mu)^N (1 - k(i, \mu))^2, \end{aligned} \quad (13)$$

where, P is the internal reflection transfer function. Since $k < 1$, P decreases for increasing N and can be neglected for $N > 2$.

Composite Appearance of a Raindrop. The composite appearance is now obtained by substituting R , S and P from Eqs. (9), (11) and (13), into Eq. (5):

$$\begin{aligned} L(\hat{n}) &= (1 - k(i, \mu))^2 L_e(\hat{r}) + k(i, \mu) L_e(\hat{s}) \\ &+ \sum_{N=1}^2 k(i, \mu)^N (1 - k(i, \mu))^2 L_e(\hat{p}). \end{aligned} \quad (14)$$

The direction of the vectors \hat{r} , \hat{s} , \hat{p} are obtained from Eqs. (7), (10), and (12) respectively. The above equation provides a complete model for the appearance of a stationary raindrop. To illustrate the relative contribution of refraction and reflection in determining a drop's appearance, in Fig. 5 we plot the radiance of a surface point due to reflection, refraction and internal reflection ($N = 1$ and $N = 2$) as a function of distance ρ (see Fig. 5(a)). For illustration purposes, we assume orthographic projection ($\alpha = 0$) and uniform environmental radiance of ($L_e = 1$). From Fig. 5 we see that the radiance of the drop is mainly due to the refraction. In fact a raindrop transmits 94% of the incident radiance towards the camera. Specular and internal reflection are only prominent at the periphery of the drop.⁸ Hence, the appearance of the raindrop is mainly decided by refraction through the drop. We now verify the geometric and photometric models experimentally.

Verification of Geometric Mapping. Figure 6(I)(a) shows the experimental setup used for verifying the geometric mapping. An acrylic ball ($\mu = 1.49$) of radius

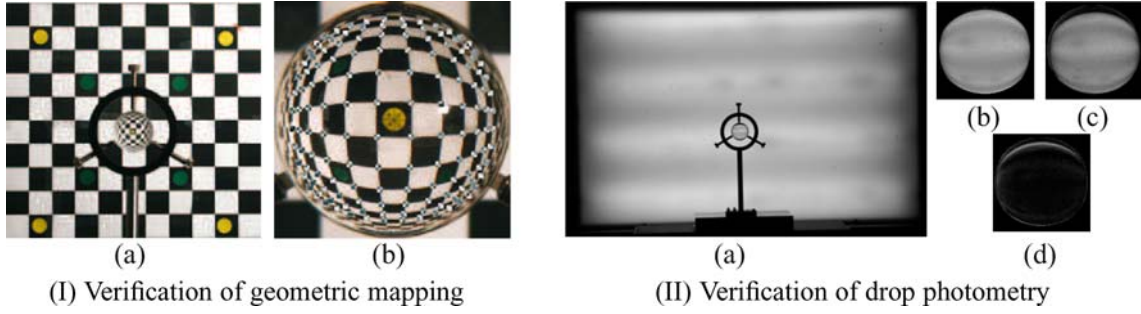


Figure 6. I(a) Experimental setup to verify the geometric mapping due to refraction. An acrylic ball was placed in front of the checkerboard pattern. I(b) The computed locations (using Eq. (7)) of the corners (checkerboard) are shown as black-white squares overlaid onto the captured image. The percentage RMS error is 1% of the diameter of the sphere (in pixels). II Verification of the photometry of refraction through a drop. II(a) An acrylic ball was placed in front of a calibrated light box. II(b) The image computed using the photometric model in Eq. (9). II(c) The image of the acrylic ball. II(d) Differences (in gray levels) between the actual image II(b) and the predicted image II(c). The RMS error was 3 gray levels (out of 256).

0.875 inches was placed 6 inches in front of the checkerboard pattern and imaged from a distance of 85 inches. To verify the mapping, we computed the locations of checkerboard corners within the image of the ball using Eq. (7) and compared it with the actual locations of the corners. Figure 6(I)(b), shows the computed corners (small black-white squares) overlaid onto the captured image. The percentage RMS error in the mapping is found to be 3.5 pixels, which is less than 1% of the diameter of the sphere (in pixels). The small error in the result is mainly due to the assumptions of orthographic projection and the distant background. Nevertheless, the result verifies the accuracy of our model.

Verification of Drop Photometry. In Fig. 6(II)(a) we show the experimental setup used for verifying the photometric model of refraction.⁹ The acrylic ball of radius 0.875 inches was placed 9 inches from a calibrated light box. Figure 6(II)(b) shows the image computed using the photometric model in Eq. (9) while Fig. 6(II)(c) shows the actual image obtained from a camera with a linear radiometric response. Figure 6(II)(d) shows the absolute values of the differences in the gray levels of the predicted and the calculated values. The RMS error is 3 gray levels

(out of 256). The error at the upper edge of the acrylic ball in Fig. 6(II)(d) is due to misalignment of the camera's optical axis with the horizontal direction.¹⁰ Except in this upper region, the intensity difference is almost zero across the image. This verifies the accuracy of our photometric model.

4.2.2. Capturing the World in a Drop. A raindrop refracts light from a wide range of angles into the camera. The field of view of a drop can be obtained using Eq. (7) by calculating the maximum permissible value of θ_r over all possible angles θ_n (i.e. $0 \leq \theta_n \leq 90^\circ$). It is easy to verify that the **field of view of the raindrop is approximately 165°** . Note that a typical fish-eye lens has a very similar field of view. Therefore, when it rains, each raindrop that is within the depth of field of the imaging system produces a wide angle view of the environment. In short, rain results in numerous *natural* omni-directional imaging systems that project the world onto the same image plane, albeit at a very low resolution. Since we know the geometric mapping of the environment due to a raindrop, we can use it to undo distortions in the wide angle view produced by a drop to obtain perspective views. This is illustrated in Fig. 7 where we have created near-perspective

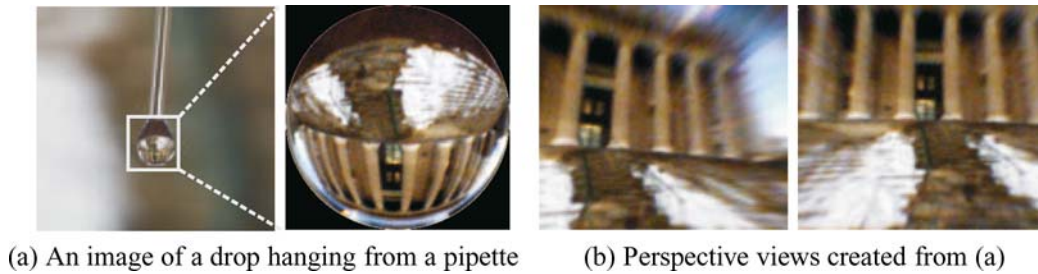


Figure 7. Looking at the world through a raindrop. (a) An image of a drop hanging from a pipette and a magnified version. (b) Near-perspective views computed using the geometric mapping due to refraction. Note that, in the perspective views, straight lines in the scene are mapped to straight lines in the image.

views of the scene as shown in Fig. 7(b) from an image of drops as shown in Fig. 7(a). One may take this notion of the “world in a drop” one step further by observing that two drops in the field of view provide two distinct views of the same scene that can be used to compute the structure of the scene.

4.2.3. Average Brightness of a Stationary Raindrop.

At normal low resolution, drops are just a few pixels wide and their complex appearance is generally lost. At this resolution only the average brightness of raindrops is relevant. Nevertheless, the developed geometric and photometric models give some interesting insights into the brightness properties of a raindrop:

- Raindrops refract light from a large solid angle (165°) of the environment (including the sky) towards the camera. Moreover, the incident light that is refracted is only attenuated by 6%. Specular and internal reflections further add to the brightness of the drop. Thus, a drop tends to be much brighter than its background (the portion of the scene it occludes).
- The solid angle of the background occluded by a drop is far less than the total field of view of the drop itself (see Fig. 8(a)). Thus, in spite of being transparent, the average brightness within a stationary drop (*without motion-blur*) does not depend strongly on its background.
- The brightness of a raindrop is not affected by other raindrops. This is because for any given raindrop the total solid angle subtended by other raindrops (raindrops are small and are far apart) is insignificant to that subtended by the environment.

We verified the first two observations using a video of drops falling under an overcast sky. The video was captured at 30 frames per second using a Canon Optura video camera. A short exposure time of 1 ms was used to prevent motion blur of drops. The background scene consisted of horizontal stripes of different brightnesses, as shown in Fig. 8(b). The average intensities of drop-sized regions marked A through E are plotted as a function of time. Each spike corresponds to a sudden increase in brightness when a drop passes through the marked region. Note that the brightnesses of the drops (peak values of the spikes) are much higher than the corresponding background intensities. Also, these peak values are approximately the same even though the background intensities are very different (see the dashed line in Fig. 8(b)). We will now use these properties of raindrops to model the motion-blurred intensities of a falling drop.

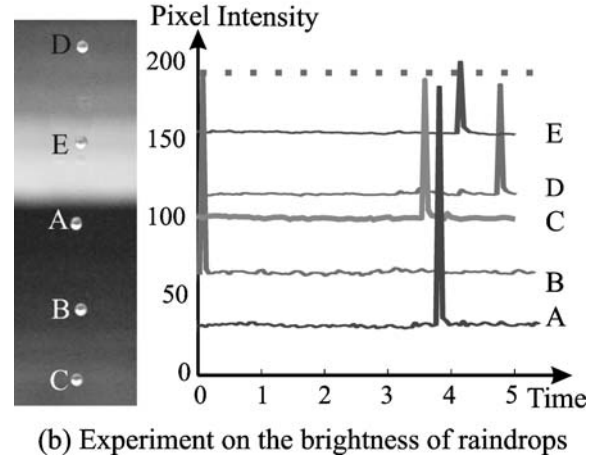
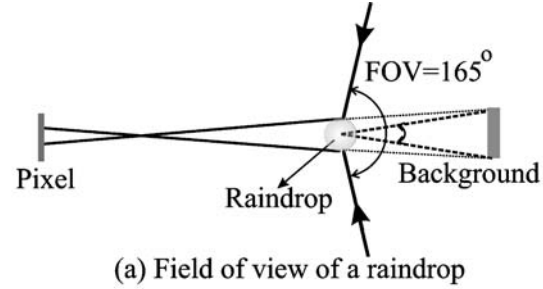


Figure 8. Geometry and brightness of a raindrop. (a) The solid angle subtended by the background occluded by a drop is much smaller compared to its large field of view of 165° . (b) Experiment verifying the average brightnesses of raindrops. The background is a plane with 5 horizontal stripes of different shades of gray. The average intensities produced in the drop-sized regions A through E are plotted as a function of time. Note that the drops (spikes) are brighter than their backgrounds. Further, in the absence of motion-blur, the brightnesses of the drops are roughly the same and independent of the background.

4.3. Photometry of Rain Streaks: Motion Blur

Motion-blur significantly affects the appearance of rain. To illustrate this we show two images of a scene in rain, one taken with a short exposure time of 1 ms (see Fig. 9(I)(a)), and the other with a normal exposure time of 30 ms (see Fig. 9(I)(b)). As seen in Fig. 9(I)(a), stationary raindrops are very bright and they do not appear transparent. However, at long exposures, due to fast motion, raindrops produce severely motion-blurred rain streaks. Interestingly, it is the fast motion of drops that makes it look transparent. Unlike a stationary drop, the intensities of a rain streak depend on the brightness of the drop as well as the background scene radiances and integration time of the camera. Let us now analyze these dependencies.

Consider a video camera with a linear radiometric response and exposure (integration) time T , observing a scene with rain. To determine the intensity I_r produced at a pixel effected by a raindrop, we need to examine

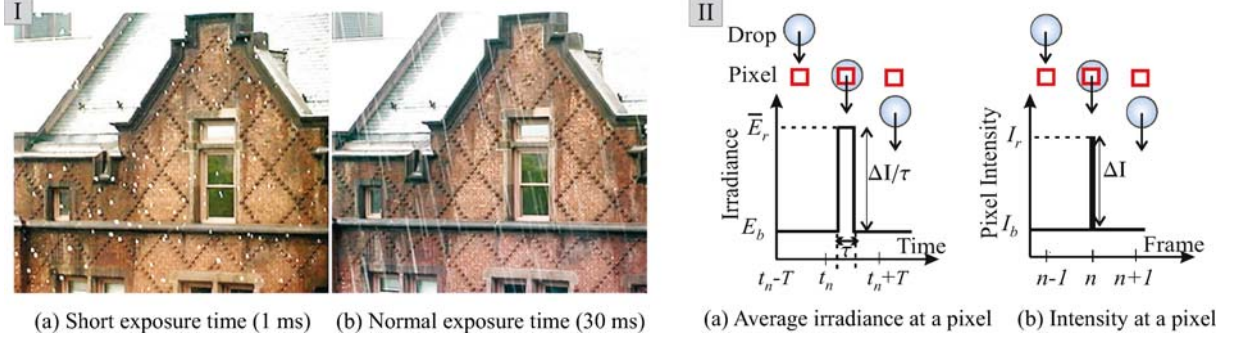


Figure 9. (I) Raindrops and motion-blur. An image of a scene taken in rain with (a) a short exposure time of 1 ms and (b) with typical exposure time of a camera (30 ms). (II) The intensities produced by motion-blurred raindrops. II (a) The average irradiance at the pixel due to the raindrop is \bar{E}_r and that due to the background scene is E_b . Note that $\bar{E}_r > E_b$. The drop projects onto a pixel for time $\tau < 1.18$ ms, which is far less than the typical exposure time T of a camera. (b) Intensities of a pixel in three frames. A drop stays over the pixel in only a single frame and produces a positive intensity fluctuation of unit frame width.

the irradiance of the pixel over the time duration T . Figure 9(a) shows a raindrop passing through a pixel within the time interval $[t_n, t_n + T]$. In Appendix 10.2, we show that the time τ that a drop projects onto a pixel is far less than T . Thus, the intensity I_r is a linear combination of the irradiance E_b due to the background of the drop and the irradiance E_r due to the drop itself:

$$I_r(\vec{r}) = \int_0^\tau E_r dt + \int_\tau^T E_b dt. \quad (15)$$

Here, we have dropped the parameters (\vec{r}, t) on the right hand side for brevity. If the motion of the background is slow, E_b can be assumed to be constant over the exposure time T . Then, the above equation simplifies to

$$I_r = \tau \bar{E}_r + (T - \tau) E_b, \quad \bar{E}_r = \frac{1}{\tau} \int_0^\tau E_r dt, \quad (16)$$

where, \bar{E}_r is the time-averaged irradiance due to the drop. For a pixel that does not observe a drop, we have $I_b = E_b T$. Thus, the change in intensity ΔI at a pixel due to a drop is

$$\Delta I = I_r - I_b = \tau (\bar{E}_r - E_b). \quad (17)$$

Recall from Section 4.2.3 that raindrops are much brighter than their backgrounds. Thus, $\bar{E}_r > E_b$ and ΔI is positive. Substituting $I_b = E_b T$ in Eq. (17), we obtain a relation between ΔI and I_b :

$$\Delta I = -\beta I_b + \alpha, \quad \beta = \frac{\tau}{T}, \quad \alpha = \tau \bar{E}_r. \quad (18)$$

In Appendix 10.2, we derive the time τ for which a drop remains within a pixel as a function of the physical

properties of the drop (size and velocity). Also, we show that τ and hence β are constant for all pixels within a streak. In addition, since the brightness of the (stationary) drop is weakly affected by the background intensity, the average irradiance \bar{E}_r can be assumed to be constant for pixels that lie on the same streak (see Section 4.2.3). Thus, the change in intensities ΔI observed at all pixels along a streak are *linearly* related to the background intensities I_b occluded by the streak.

In Appendix 10.2, numerical bounds are also derived for the parameters β and τ . We show that the maximum value of τ is approximately 1.18 ms, which is much less than the typical exposure time $T \approx 30$ ms of a video camera. As a result, the slope β is shown to lie within the range $0 < \beta < 0.039$. Based on these bounds, we make the following observations:

- A raindrop produces a positive change in intensity and stays at a pixel for a time far less than the integration time of a typical video camera. Thus, a drop produces a positive intensity change ($\Delta I > 0$) of unit frame width at a pixel, as illustrated in Fig. 9(b).
- The change in intensities observed at all pixels along a rain streak are linearly related to the background intensities I_b occluded by the streak, with slope β of this linear relation lying within the range $0 < \beta < 0.039$. This can be used to detect rain streaks.

The discussed photometric and dynamic models not only increase our understanding of the visual manifestations of rain but they can also be used to develop effective algorithms for detection and removal of rain from videos. These models can also be incorporated in existing outdoor vision algorithms to make them more robust to rain without explicitly removing the visual effects of rain.



Figure 10. Results of applying median filtering over time for rain removal. (a) Original frame from the movie “Magnolia”. The scene consists of a person moving and speaking on a phone and rain visible through the glass window. (b) Rain removed frame. (c) Difference between the original and filtered frame. Simple image processing techniques cannot distinguish rain from other types of signals such as scene motion and therefore alter the signal itself. For illustration purposes, the difference image has been scaled by a constant.

5. Algorithm for Detection and Removal of Rain from Videos

We now develop a simple yet effective algorithm for detection and removal of rain. One might consider the effects of rain as noise and believe that simple image processing techniques can be used to handle rain. However, unlike noise, the intensities produced by rain have strong spatial structure and depend strongly on the background brightness. Furthermore, certain type of scene motions can produce temporal and spatial frequencies similar to rain, making it hard for simple image processing techniques to distinguish rain from other signals. This is illustrated in Fig. 10 where we show the results of applying median filtering over time for rain reduction. As can be seen in Fig. 10(c) median filtering removes some rain but it also alters the signal due to motion. In addition, it is hard to track individual raindrops or learn a general appearance of rain.¹¹

To handle rain we need algorithms that can distinguish rain from other types of signals and are general enough to handle wide variations in its visual appearance. The developed photometric and dynamic models provide a simple and efficient way of achieving this. Our algorithm consists of two main stages. In the first stage (i.e. *detection*) we identify pixels affected by rain and use them to segment rain regions from the non-rain regions. In the second stage (i.e. *removal*) we remove rain from the affected pixels that lie in the rain segmented region of the video. Figure 11 shows the pipeline of the algorithm. Here we discuss these stages in detail.

5.1. Detection of Rain in Videos

Applying Constraints of the Photometric Model. Consider a video of a scene captured in rain such as the one shown in Fig. 11. We apply constraints derived using the

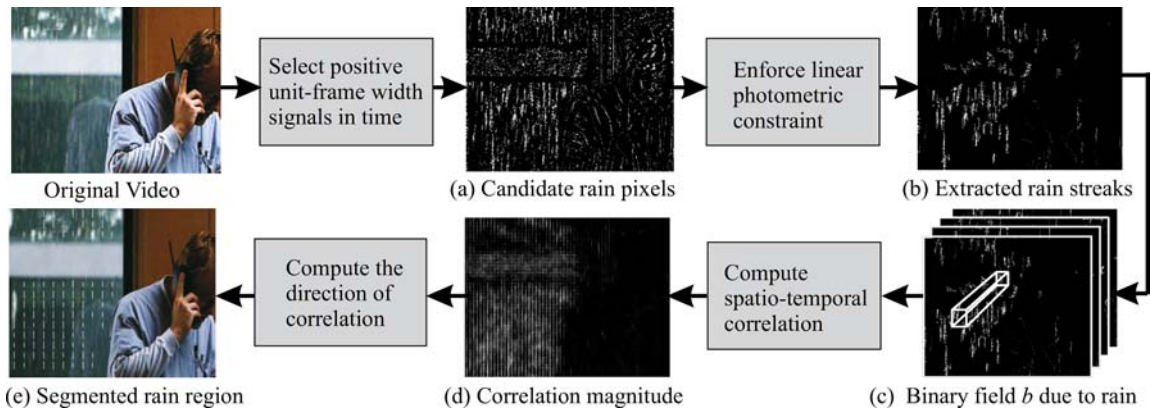


Figure 11. The rain detection algorithm applied to a video. (a) Using the photometric model to identify pixels that are affected by rain. Candidate rain pixels are shown in white. Note that there are several false positives (non-rain pixels). (b) Applying the linear photometric constraint to streak intensities (Eq. (18)). This reduces false positives significantly to yield an estimate of the binary rain field b . (c) The computation of spatio-temporal correlation in the binary field b . (d) A correlation map computed using $l = 11$ and $f = 30$ frames and by adding the correlation R_b over a (3×3) pixel neighborhood. Pixels with high intensity values represent rain pixels while the non-rain pixels have low intensity values. (e) Needle map showing the segmented rain regions and the direction of falling rain. The needle map is kept sparse for clarity.

photometric model to detect *candidate* pixels affected by rain in each frame of the video. In Section 4.3, it was shown that a drop produces a positive intensity fluctuation of unit frame duration. Hence, to find candidate rain pixels in the n^{th} frame, we need to only consider intensities I_{n-1} , I_n and I_{n+1} at each pixel corresponding to the 3 frames $n - 1$, n and $n + 1$, respectively (see Fig. 9(b)). If the background remains stationary in these three frames,¹² then the intensities I_{n-1} and I_{n+1} must be equal and the change in intensity ΔI due to the rain drop in the n^{th} frame must satisfy the constraint

$$\Delta I = I_n - I_{n-1} = I_n - I_{n+1} \geq c, \quad (19)$$

where c is a threshold that represents the minimum change in intensity due to a drop that is detectable in the presence of noise. The result of applying this constraint with $c = 3$ gray levels is shown in Fig. 11(a). The selected pixels (white) include almost all the pixels affected by rain.

In the presence of object motions in the scene, the above constraint also detects several false positives. Some of the false positives can be seen in and around the moving person in Fig. 11(a). To reduce such false positives, we apply the photometric constraint in Eq. (18) as follows. For each individual streak¹³ in frame n , we verify whether the intensity changes ΔI along the streak are linearly related to the background intensities I_{n-1} , using Eq. (18). The slope β of the linear fit is estimated. Then, streaks that do not satisfy the linearity constraint, or whose slopes lie outside the acceptable range of $\beta \in [0 - 0.039]$, are rejected. Figure 11(b) shows a significant decrease in false positives after applying this constraint. By applying these constraints to all the frames, an estimate of the binary rain field b is obtained (see Fig. 11(c)).

Applying Constraints of the Dynamics Model. Although a significant reduction in false positives is achieved using the photometric constraint, some false positives will remain. In this step, we further reduce the false positives using the dynamics model. In Section 4.1, we showed that in a binary field produced by rain, strong temporal correlation exists between neighboring pixels in the direction of rain. Using the estimated binary field b , we compute the zeroth order temporal correlation R_b of a pixel with each of its neighbors in a local $(l \times l)$ neighborhood, over a set of frames $\{n, n - 1, \dots, n - f\}$. That is, we compute $R_b(\vec{m}p, 0)$, where m_x and m_y vary from $-(l - 1)/2$ to $(l - 1)/2$ (see Fig. 4). Due to camera noise the correlation R_b of a pixel is noisy. Therefore, to obtain a better estimate, we average R_b values of neighboring (3×3) pixels. Figure 11(d) shows the summed correlation of disjoint (3×3) neighborhoods in frame n that is computed using the previous $f = 30$ frames. Bright regions indicate strong correlation. The direction

and strength of correlation is computed¹⁴ for each neighborhood center which is depicted in Fig. 11(e) as a needle map. The direction of the needle indicates the direction of correlation (*direction of the rainfall*) and its length denotes the strength of correlation (*strength of the rainfall*). The needle map is kept sparse for clarity. Weak and non-directional correlations occur at pixels with no rain¹⁵ and hence are rejected. Thus, constraints of the photometric and dynamics models can be used to effectively segment the scene into regions with and without rain, even in the presence of complex scene motions.

5.2. Removal of Rain from Videos

To remove rain we estimate the background intensities for only those pixels that are affected by rain (computed in the detection stage) and lie within the segmented rain regions. The background intensities are estimated using the following simple method. For each pixel with rain in the n^{th} frame, we replace its intensity I_n with an estimate of the background obtained as $(I_{n-1} + I_{n+1})/2$ (see Fig. 9(b)). This step removes most of the rain in the frame. However, since drop velocities are high compared to the exposure time of the camera, the same pixel may see different drops in consecutive frames. Such cases are not accounted for by our detection algorithm.¹⁶ Fortunately, it can be shown that the probability of raindrops affecting a pixel in more than three consecutive frames is negligible. In the case of a pixel being affected by raindrops in 2 or 3 consecutive frames, we remove rain by assigning the average of intensities in the two neighboring pixels (on either side) that are not affected by raindrops. Our results show that this additional step can be very effective for rain removal.

5.3. Experimental Results

We conducted experiments on several videos with rain to demonstrate the effectiveness of our algorithms. In all experiments, we chose the photometric threshold $c = 3$ gray levels and the spatio-temporal correlation was computed using $l = 11$ (i.e. (11×11) neighborhoods) over $f = 30$ frames. The rain segmentation has a temporal lag since 30 frames were used to compute spatio-temporal correlation. Please see the submitted videos (<http://www.cs.columbia.edu/cave/submit/ijcvrain>, 2006) for the results of the algorithms.

Figure 12(I)(a) shows two frames from the movie “Magnolia,”¹⁷ where a person is moving and speaking over the phone. Rain is visible through the window. The camera moves and zooms in on the person. Rain detection is made more challenging by fast moving texture (shirt creases and folds on the arm). Despite these complexities, our algorithm robustly detects only pixels with

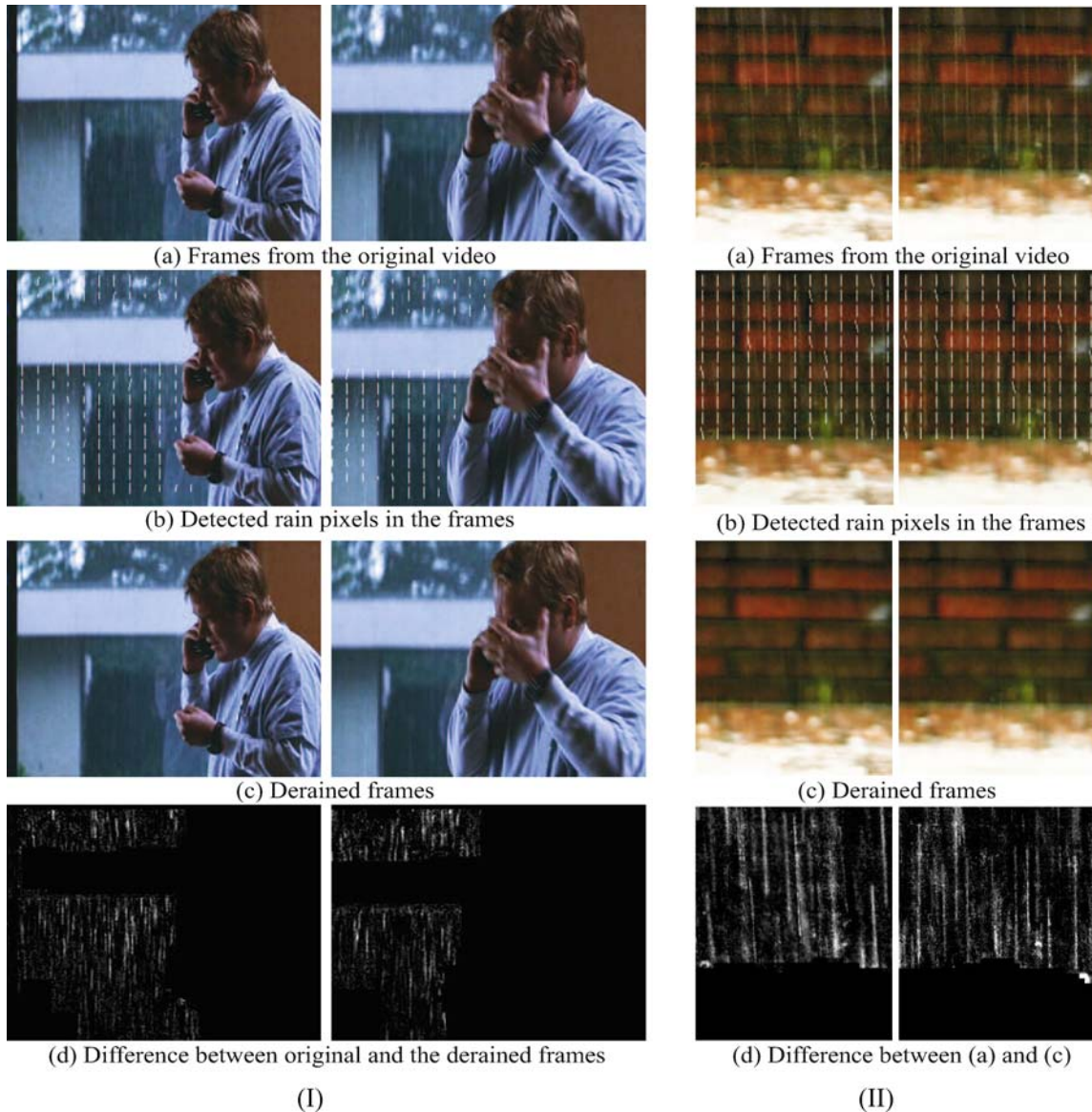


Figure 12. (I) Detection and removal of rain for a clip of the movie “Magnolia” (Original images courtesy of New Line Productions-©1999 New Line Productions, Inc.). (a) Two frames from the original video. The scene consists of a person moving and speaking on the phone and rain visible through the glass window. Fast moving textures (shirt creases and folds on the moving arm) make the detection task challenging. (b) Detected regions with rain represented as a needle map. The direction of the needle at a pixel represents the direction of rain and the length of needle represents the strength of the rain. (c) Derained frames. (d) Difference between the original frames and the derained frames. (II) In this example the rain causes ripples in the pool of water. These ripples may be viewed as a temporal texture with frequencies similar to those produced by rain. However, since the dynamic and photometric properties of rain are very different from those of the ripples, our algorithm detects only pixels with rain. For illustration purposes, the difference frames have been scaled by a constant factor. Please see the submitted videos (<http://www.cs.columbia.edu/cave/submit/ijcvrain>, 2006).

rain (see Fig. 12(I)(b)). The false positives are eliminated as a result of enforcing linear photometric and directional correlation constraints. Note that we are unable to detect rain in pixels with a bright background (white wall) because the changes in intensities produced by rain are very low in these regions. Derained frames are shown in Fig. 12(I)(c) and the differences between the derained and original frames (scaled by a constant) are shown in Fig. 12(I)(d). Compare our results with that

obtained using a simple image processing technique (median filtering over time) as shown in Fig. 10. Unlike image processing techniques, our algorithm only removes the rain signal, thus giving better results. In Fig. 12(II) we show results for a scene with raindrops falling and forming a pool of water. The ripples of water may be viewed as a temporal texture with frequencies similar to those produced by rain. Since our algorithm accounts for the photometric and dynamic properties of rain, it

is able to distinguish rain from ripples as can be seen from the segmentation results in Fig. 12(II)(b). The de-rained frames are shown in Fig. 12(II)(c). These examples demonstrate that our algorithm is effective for scenes with motion and at the same time is insensitive to time-varying textures that have temporal frequencies similar to those of rain.

5.4. Discussion

Detection and removal of rain is a challenging problem, given that background and scene motion vary rather widely and may have fast textured motion. In spite of these difficulties, by modeling the visual appearance of rain we have developed a robust algorithm for rain detection and removal. However, our algorithm has certain limitations.

Our algorithm can only remove streaks that can be detected. Severely defocused streaks and streaks on bright backgrounds produce very small changes in intensities that are difficult to detect in the presence of sensor noise. Hence, we are unable to remove such streaks. In addition, we do not handle the steady¹⁸ effects of rain for which defogging algorithms (Narasimhan and Nayar, 2002) can be used. Since we use several frames (about 30 frames) our technique for rain segmentation is robust to background motion. However, in extreme cases where the background exhibits fast repeated motion for long periods of time, we may not be able to segment rain regions and hence successfully remove rain. In future work, we wish to develop further analysis that will overcome this limitation.

6. Analysis of the Visibility of Rain

The post-processing algorithm is useful for handling rain when the video has already been acquired or when we have no control over camera parameters during video capture. In many cases, however, we have control over the camera parameters, as in most vision applications. In such scenarios is it possible to reduce or remove the visual effects of rain during the image acquisition? In order to address this, we have analyzed how various factors, such as camera parameters, properties of rain and scene brightness, affect the appearance of rain in images and videos. We derive these dependencies and experimentally verify them. Our analysis shows that the unique properties of rain—its small size, fast velocity and spatial distribution—make the visibility of rain strongly dependent on camera parameters. This dependence allows us to reduce/remove the visibility of rain during image acquisition by simply setting the optimal camera parameters. This can be achieved without altering the appearance of the scene. The parameters of a camera can also be set

to enhance the visual effects of rain. This can be used to develop an inexpensive and portable camera-based rain gauge that provides instantaneous rain rate measurements. In addition, this technique can be used to control the visual effects of rain during the filming of movies.

We begin by quantitatively defining a way to measure the visibility of rain. Figure 13(I)(a) shows a frame from a video of a static scene taken in rain. The effects of rain are clearly visible. The plot below shows the intensity fluctuations produced by rain at a pixel. Note that the signal exhibits a large variance over time. Figure 13(I)(b) shows a frame from a video of the same scene, under identical environmental conditions, taken with camera parameters set to reduce the visual effects of rain. Here, the effects of rain are not visible. The variation in intensity at the same pixel is now low. Thus, variance at a pixel over time is a good indicator of the visibility of rain and can be used as a quantitative measure of it.¹⁹ We will now derive analytical expressions that relate the variance (visibility) to various factors such as the camera parameters, the properties of rain, and the scene brightness. To do this we first model the intensities produced by individual drops and then consider the effects due to a volume of rain.

6.1. Camera Parameters and Intensity of a Raindrop

Raindrops are motion-blurred and defocused due to the finite exposure time and limited depth of field of a camera, respectively. In this section, we analyze how the intensities of these motion-blurred and defocused streaks depend on camera settings. This is later used to model the effects due to a volume of rain. For deriving these intensities we assume the camera to have a linear radiometric response. The intensity I at a pixel is related to the radiance L as Horn (1986),

$$I = k \frac{\pi}{4} \frac{1}{N^2} T L = k_0 L \quad (20)$$

where, k is the camera gain, N is the F-number, and T is the exposure time. The gain k can be adjusted so that image intensities do not depend on specific N and T settings. That is, $k \frac{\pi}{4} \frac{T}{N^2}$ is constant and is denoted by k_0 . We now model the change in intensities produced by rain streaks.

Raindrops and Exposure Time. Figure 13(II)(a) shows a pixel looking at raindrops that lie at different distances, z , from the camera. Drops close to the camera ($z < z_m$) project to a size larger than a pixel, where $z_m = 2 f a$ (a is the radius of the drop and f is the focal length in pixels). The change in intensity ΔI produced by these

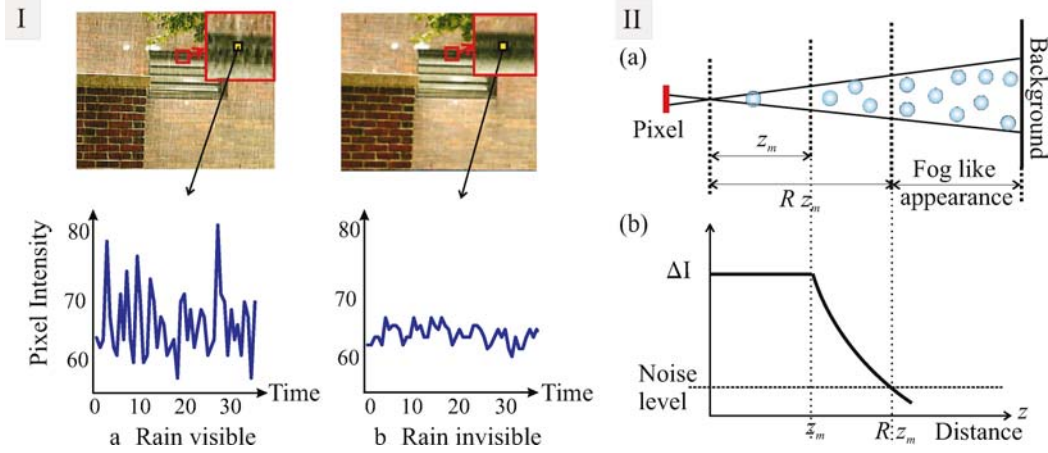


Figure 13. Dynamic weather and visibility: (I)(a) Frame from a video of a scene where rain is visible. The intensity variation due to rain is high. (b) Frame from a video of the same scene taken with camera parameters to reduce the visibility due to rain. The intensity at the same pixel shows low variance over time. (II) The change in intensity produced by a falling raindrop as a function of the drop's distance z from the camera. The change in intensity ΔI does not depend on z for drops that are close to the camera ($z < z_m$). While for raindrops far from the camera ($z > z_m$), ΔI decreases as $1/z$ and for distances greater than $R z_m$, ΔI is too small to be detected by the camera. Therefore, the visual effects of rain are only due to raindrops that lie close to the camera ($z < R z_m$) which we refer to as the *rain visible region*.

drops can be shown (from Eq. (17)) to be

$$\Delta I = I_r - I_b = k_0 \frac{\tau}{T} (L_r - L_b), \quad (21)$$

where, I_r is the motion-blurred intensity at a pixel affected by rain, and $I_b = k_0 L_b$ is the intensity at a pixel not affected by rain (i.e. the background intensity). L_r and L_b are the brightnesses of the raindrop and the background, respectively, and T is the exposure time of the camera. $\tau \simeq 2a/v$ is the time that a drop stays within the field of view of a pixel and v is the drop's fall velocity. From the above equation we see that change in intensity produced by drops in region $z < z_m$ decreases as $1/T$ with exposure time and does not depend on z .

On the other hand, the change in intensity produced by drops far from the camera that is $z > z_m$ is given by (see Appendix 10.3(a) for derivation)

$$\Delta I = k_0 \frac{4fa^2}{zv} \frac{1}{T} (L_r - L_b). \quad (22)$$

As in the previous case ΔI decreases inversely with exposure time. However, now ΔI also depends on the drop's distance from the camera, and decreases as $1/z$.

Figure 13(II)(b) illustrates how the change in intensity ΔI produced by a falling raindrop is related to its distance from the camera. The change in intensity is almost constant for distances less than $z_m = 2fa$. For $z > z_m$ the intensity fluctuation decreases as $1/z$ and for distances greater than $R z_m$ (where R is a constant), the fluctuation ΔI becomes too small to be detected by a camera.²⁰ Hence, the visual effects of rain are only produced by

raindrops in the region $z < R z_m$. We refer to this region ($0 < z < R z_m$) as the *rain visible region*. The value of R depends on the brightness of the scene and camera sensitivity.

Raindrop and Depth of Field. We now analyze the effects of a limited depth of field on the intensity produced by raindrops. We can approximate defocus as a spreading of change in intensity produced by a focused streak uniformly over the area of a defocused streak.²¹ Hence, the change in intensity ΔI_d due to a defocused drop is related to the change in intensity ΔI of a focused streak as

$$\Delta I_d = \frac{A}{A^d} \Delta I = \frac{w(v_i T)}{(w + b_c)(v_i T + b_c)} \Delta I, \quad (23)$$

where, A and A^d are the areas of the focused and the defocused rain streak, respectively, w is the width of the focused drop in pixels, b_c is the diameter of the defocus kernel (blur circle) (Horn, 1986), v_i is the image velocity of the drop, and T is the exposure time of the camera. Since raindrops fall at high velocity we can assume that $v_i T \gg b_c$. Hence, the above expression simplifies to

$$\Delta I_d = \frac{w}{w + b_c} \Delta I. \quad (24)$$

Substituting ΔI from Eq. (21) we get the intensity due to a defocused drop in the region close to camera ($z < z_m$). Intensities of defocused drops far from the camera ($z > z_m$) are obtained by substituting²² $w = 1$ and ΔI from Eq. (22) in the above equation.

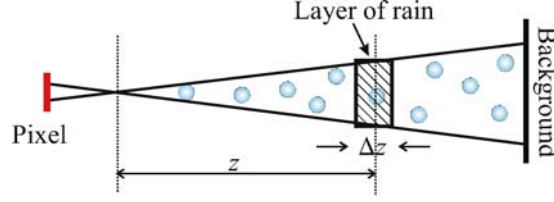


Figure 14. Intensity fluctuations produced by a volume of rain. To model the volumetric effects we partition the volume into thin layers. The intensity properties of the layers are then summed to obtain the total effect due to a volume.

6.2. Camera Parameters and Volume of Rain

Consider a camera looking at a distribution of raindrops in a volume, as shown in Fig. 14. This distribution of falling drops in 3D maps to the 2D image plane via perspective projection. As a result, multiple drops at different depths may project to the same pixel during the exposure time of the camera, producing intensity variations much larger than those of individual drops. To model these volumetric effects, we partition the volume into thin layers of rain of thickness Δz , as shown in Fig. 14. We first compute the variance due to a single layer of rain. The variance due to a volume of rain is then the sum of the variances due to the different layers. In Appendix 10.3(b), we have shown that variance $\sigma_r^2(I, z)$ due to a single layer of rain at distance z is given by

$$\sigma_r^2(I, z) = \bar{n}(z) w^d(z) \Delta I_d^2(z), \quad (25)$$

where, $\bar{n}(z)$ is the mean number of drops in the layer that pass through a pixel's field of view during the exposure time of the camera and is given by Eq. (31), $w^d(z) = w(z) + b_c(z)$ is the width of the defocused streak due to a raindrop at depth z , and $\Delta I_d(z)$ is the change in intensity produced by it (see Eqs. (24)). Substituting the values of \bar{n} , w^d and ΔI_d we get the variance $\sigma_r^2(I, z)$ due to a layer

of rain as

$$\sigma_r^2(I, z) dz = k_0^2 \frac{4a^4 \rho (L_r - L_b)^2}{v T} \frac{f dz}{z(w(z) + |b_c(z)|)}, \quad (26)$$

where, a is the size of the drop, ρ is the drop size density, v is the velocity of the drop and $w(z) = \max(\frac{fz}{a}, 1)$.

Since layers are non-overlapping and independent, the variance $\sigma_r^2(I, z)$ due to different layers can be added to find the variance due to a volume of rain. Substituting for $w(z)$, $b_c(z)$, and integrating the above equation over z , we obtain the variance and hence the standard deviation $\sigma_r(I)$ due to a volume of rain as,

$$\sigma_r(I) = \frac{k_0}{\sqrt{T}} \frac{a^2 \sqrt{\rho}}{\sqrt{v(a)}} (L_r - L_b) \sqrt{\mathcal{G}(f, N, z_0)}, \quad (27)$$

where, $\mathcal{G}(f, N, z_0)$ is a function (see Appendix 10.3(c) for exact form) of focal length f , F-number N , and the distance z_0 of the focus plane. Equation (27) shows that the visibility (σ_r) of rain increases as the square of the size a of the raindrop and as square root of density ρ of rain. The visibility also decreases linearly with background brightness L_b .

The dependence of the visibility of rain (i.e. σ_r) on camera parameters, is shown in Fig. 15(a)–(c).

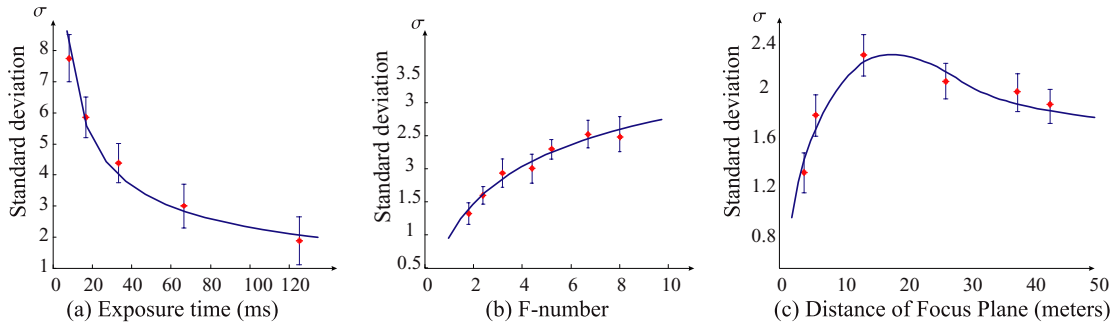


Figure 15. Experimental verification of the analytical model that relates visibility of rain σ_r to camera parameters. The solid curves show σ_r as given by Eq. (27). The red marks show the mean values of the measured σ_r and the error bars show the uncertainty in measurement. (a) σ_r as a function of exposure time T . The time T is varied from 8 ms to 125 ms with other camera parameters kept fixed at ($f = 3155$, $N = 5.6$, $z_0 = 10$). The experiment verifies the $1/\sqrt{T}$ dependence on exposure time. (b) The visibility dependence on aperture size (F-number). The F-number N was increased from 1.8 to 8. Other camera parameters were set to ($f = 8000$, $T = 16$, $z_0 = 14$) (c) Dependence of visibility on distance of the focal plane z_0 . The focal plane was kept at different distances from the camera from $z_0 = 4$ m to $z_0 = 40$ m while other parameters were kept fixed ($f = 8000$, $T = 16$, $N = 6.7$). In all the above cases the experimental values show close agreement with the values predicted by our models.

Figure 15(a) shows that the visibility of rain decreases as $1/\sqrt{T}$ with exposure time of the camera. Figure 15(b) shows that σ_r initially increases rapidly with F-number N and then reaches saturation for higher F-numbers. Figure 15(c) shows the σ_r dependence with respect to distance z_0 of the focal plane. The curve shows a maximum at the location of the focus plane that keeps the largest possible region of rain in focus. We conducted experiments to verify these dependencies on camera parameters. A Canon XL1 camera was used in our experiments. The camera was calibrated to make its radiometric response linear.²³ The standard deviation σ_r for a given camera setting was computed by taking videos of rain (200 frames) against a stationary background of uniform brightness. 1800 pixels²⁴ were used to estimate the variance. The red marks in Fig. 15(a)–(c) show the mean values of the measured σ_r and error bars show the uncertainty in the measurement of σ_r . The measured variances are in close agreement with the values predicted by our model. For details regarding the camera settings for specific experiments please see the caption of Fig. 15. These experiments validate the correctness of the derived analytical model.

7. Rain Reduction/Removal Using Camera Parameters

We now show how this analysis can be used to reduce the effects of rain. Although changing camera parameters may affect scene appearance, in typical scenes, there is some flexibility in setting camera parameters. This flexibility can be used to remove rain without affecting scene appearance. We present some common scenarios where rain produces strong effects and offer techniques to reduce them. Please see the submitted videos (<http://www.cs.columbia.edu/cave/submit/ijcvrain>, 2006). All the experiments were done with a radiometrically calibrated Canon XL1 camera. The camera gain was set on the automatic mode to maintain the average brightness of the scene constant over different camera settings.

Reducing Rain Using Depth of Field. Figure 16(I)(a) shows a frame from a traffic scene video. Since the scene has fast moving objects, a short exposure time $T = 8$ ms is required, which increases the degradation due to rain. However, the scene is far from the camera and has small depth variations. Our analysis shows that for such types of scenes the visibility of rain can be reduced by a factor of 0.4944 (Eq. (27)) by decreasing the F-number from its default value of $N = 12$ to $N = 2.4$. Figure 16(I)(b) shows a frame from a video of the same scene taken with F-number $N = 2.4$. Note that rain effects are significantly reduced (see the magnified image regions that are shown in full resolution) while scene appearance has not

changed. The measured reduction in rain visibility (σ_r) due to the change in N is 0.4541 (error margin = 0.0884), which is close to the predicted value of 0.4944.

Reducing Rain Using Exposure Time. Figure 16(II)(a) shows a frame from a video of people walking on a sidewalk. Unlike the previous example, this scene has slow motion (less than 15 pixels/sec). However, the scene is close to the camera (lies in the rain visible region $z < R z_m$) and has a large depth range, hence a large F-number $N = 14$ is needed to capture the scene. The effects of rain are strong in such a scenario, as can be seen in Fig. 16(II)(a). For this type of scene our analysis suggests that the visibility of rain can be reduced by a factor of 0.5 (see Eq. (27)) by increasing the exposure time from the default value of 16 ms to 66 ms. As seen in Fig. 16(II)(b), the visual effects of rain are almost removed without affecting the scene appearance. The measured reduction in rain visibility is 0.4615 (error margin 0.0818), which is close to the predicted value of 0.5.

Reducing Rain Using Multiple Parameters. Figure 16(III)(a) shows a scene with moderate depth variation and motion taken with default camera parameters—exposure time $T = 16$ ms and F-number $N = 12$. For such scenarios the visibility of rain can be reduced by increasing the exposure time to $T = 33$ ms and decreasing the F-number to $N = 6$. Figure 16(III)(b) shows a frame from a video taken with these camera settings. The effects of rain are considerably reduced. The measured reduction in rain visibility is 0.5496 (error margin 0.094), and is close to the predicted value of 0.4944.

Reducing Heavy Rain. Figure 16(IV)(a) shows a frame from a video of a scene in heavy rain taken with default camera parameters—exposure time $T = 16$ ms and F-number $N = 4$. Despite the strong visual effects of rain we can significantly reduce the effects of rain by setting exposure time to 120 ms, as seen in Fig. 16(IV)(b). The measured reduction in rain visibility is 0.3763 (error margin 0.0824) which is close to the predicted value of $\sigma_r = 0.3536$.

Implication for Outdoor Vision Systems. Our method of reducing rain can significantly improve the performance of many outdoor vision systems. To illustrate this, we show the results of applying a well known implementation (Birchfield, 2005) of feature detection and tracking algorithm (Lucas and Kanade, 1981) on two panning video sequences taken in rain under similar lighting and environmental conditions. One of the videos is acquired with default camera parameters $N = 12$ and $T = 16$ ms and the other with aperture N set to optimal value of 4 for reducing rain. For each video, 600 best features are



Figure 16. Some common scenarios where rain produces strong effects and our results on rain reduction/removal. The frames in column (A) show the scene captured with default camera parameters (camera parameters set automatically by the camera for a given scene). The frames in column (B) show the same scene (with identical environmental conditions) taken with camera parameters estimated by our method to reduce rain visibility. (I) A traffic scene in rain with fast moving objects but low depth variation. (II) A scene with people walking on a sidewalk. The scene has large depth variation but slow motion. (III) People walking on stairs. The scene has moderate depth range and motion. (IV) A scene with heavy rain. Note that in all these cases the effects of rain were reduced during image acquisition and no post-processing was needed. Also, the visual effects of rain were reduced without affecting the scene appearance. Please see the submitted videos (<http://www.cs.columbia.edu/cave/submit/ijcvrain>, 2006).

automatically selected from the initial frame in a specified region²⁵ and then tracked over the video sequence. In the case of video taken with default camera settings only 37 features are tracked successfully, as seen in Fig. 17(a). In contrast, 400 features (see Fig. 17(b)) are tracked successfully in the rain reduced video. This result shows how rain can severely impair the performance of a feature detection and tracking algorithm and the improvement that

can be achieved using our method. The results have implications for other outdoor vision algorithms.

These experiments demonstrate the effectiveness of reducing rain by setting appropriate camera parameters. Also, since our method does not require post-processing it can be easily incorporated as a feature into consumer cameras. As an example, Table 1 shows the camera parameters for the Canon XL1 that should be used to

Table 1. This table shows how our results can be incorporated as a feature into commercial video cameras to reduce the effects of rain. The camera parameters given here are for the Canon XL1 video camera. The scene is described using a coarse estimate of the scene properties—motion (image velocities), near distance, and its depth range. These scene properties can be manually set by the user or estimated automatically by the camera itself. Once the scene properties are determined, using a lookup table similar to this one, camera parameters can be set to reduce rain.

Scene motion	Near distance	Depth range	Exposure time (ms)	F-number	Scene motion	Near distance	Depth range	Exposure time (ms)	F-number
(a) slow	close	large	66	14	(e) fast	close	large	X	X
(b) slow	close	small	33	4.4	(f) fast	close	small	X	X
(c) slow	far	large	66	6	(g) fast	far	large	8	6
(d) slow	far	small	33	2	(h) fast	far	small	8	2.4

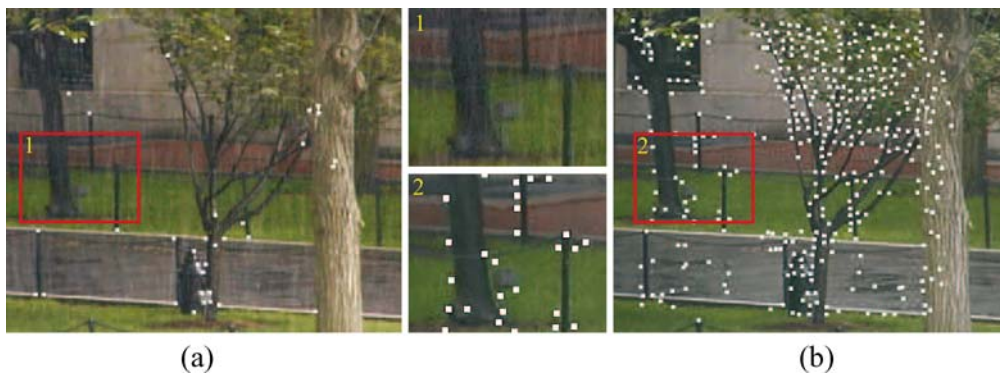


Figure 17. Results of feature detection and tracking in a panning video sequence taken in rain with (a) default camera parameters ($T = 16$ ms, $N = 12$) and (b) with optimal camera settings ($T = 16$ ms, $N = 4$) for reducing rain. In both sequences, 600 best features are automatically selected by the algorithm and then tracked over 117 successive frames. Due to rain, only 37 features are tracked successfully in video taken with default camera settings, while 400 features are successfully tracked in video taken with optimal camera settings. Please see submitted videos (<http://www.cs.columbia.edu/cave/submit/ijcvrain, 2006>).

reduce the visual effects of rain for various types of scenes. Only a coarse estimation of scene properties is needed.²⁶ We categorize scene distances as *close* or *far*, depending on whether the scene distance is less than or greater²⁷ than Rz_m . Similarly, we need a coarse estimate for scene motion. Objects with image velocities of less than 15 pixels/sec are considered slow, i.e., no motion-blur is observed if the exposure time is set to 1/15 of a second or higher.

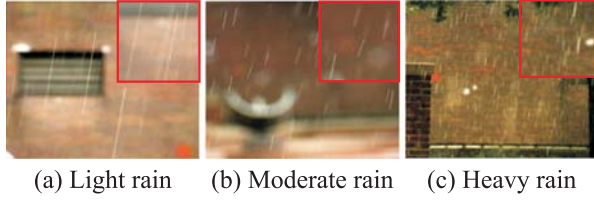
Discussion. Our analysis enables us to reduce the visual effects of rain during image acquisition by simply setting appropriate camera parameters. Note that changing the exposure time and aperture can affect the image intensities (see Eq. (20)). However, most cameras have automatic gain control which allows one to change these camera settings without significantly affecting the brightness of the image. If we do not have control over camera parameters, the post-processing algorithm can be used to handle rain. Here we discuss some of the benefits and limitations of the method.

Reducing rain during image acquisition allows us to exploit the limited depth of field of a camera to defocus raindrops close to the camera, while maintaining the

scene in focus. In contrast, this depth information is lost once an image is captured and hence cannot be used in post-processing algorithms. Also, since the method reduces rain from each frame independently, it can also be used for reducing rain from still images. Despite these benefits, there are certain limitations. The method will not be able to reduce rain in scenes with very fast motion and when objects are very close to the camera, cases that correspond to rows (e–f) in Table 1. Increasing the exposure time or decreasing the depth of field in such scenes might not be possible without affecting the scene appearance. Also, the method is not as effective in reducing very heavy rain. In such cases the post-processing technique described in Section 5 might be required.

8. Camera-Based Rain Gauge

We now show how the visual effects of rain can be enhanced to develop a camera-based rain gauge,—a device that measures rain rate. The camera-based rain gauge provides instantaneous rain rate measurements (time scale of seconds) and is robust to camera and background scene motion.



Type of Rainfall	Camera parameters (f, N, z_0, T)	Rain rate mm/hr	
		Measured	Reported
(a) Light	(7095, 3.8, 3, 16)	1.34	0.763
(b) Moderate	(5148, 4.4, 3, 4)	3.215	2.28
(c) Heavy	(3300, 1.8, 3, 4)	14.28	11.17

Figure 18. Frames from a camera-based rain gauge for different types of rainfall (a) Light rain. (b) Moderate rain (c) Heavy rain. A comparison of rain rate measured by the camera-based rain gauge to the reported hourly rain rate obtained from the National Climatic Data Center (NCDC). The differences in rain rate measurements are expected due to the distance of a few miles between measuring locations and differences in time scale (seconds vs hours) at which rain rates are measured.

The camera-based rain gauge measures rain rate by observing the size and the number of drops in a small volume of rain over time. This volume is defined by the F-number and the distance of the focal plane z_0 . To reduce the chances of rain streaks overlapping over each other, the camera is set to have a low depth of field. The value of z_0 is set so that the smallest raindrops are visible, that is $z_0 \leq 2f a_{min}$, where f is the focal length and $a_{min} = 0.5$ mm is the radius of the smallest raindrop. As z_0 is known, we can then determine the size and velocity of the raindrops from the focused rain streaks. A smaller exposure time also enhances the visibility of rain streaks.

Each frame is segmented into rain and non-rain pixels using the method described in Section 5. A linear time sequential labeling algorithm (Horn, 1986) is then used to obtain the number of raindrops, size, and velocity (length of streaks) of each drop. Defocused streaks are removed by rejecting rain streaks that do not satisfy the velocity-size relationship.²⁸ Each frame gives a count of the number of drops of a specific size in the observed rain volume. Repeating this over several frames provides a robust estimate of the number of drops of different sizes and hence the density $\rho(a)$ of rain. The total rain rate h can then be computed from the estimated $\rho(a)$ using (Wang and Clifford, 1975),

$$h = \int h(a) da = 3.6 * 10^6 \frac{4\pi}{3} \int a^3 \rho(a) v(a) da. \quad (28)$$

We conducted a number of experiments to verify the accuracy of our camera-based rain gauge. Figure 18(a)–(c) shows frames from three illustrative scenarios—(a) mild rain, (b) moderate rain, and (c) heavy rain. We computed the rain rates for these events over a short duration of 10s. The camera parameters were set to enhance the effects of rain and the rain rate measurements obtained are shown as a table in Fig. 18. The results are compared with the reported rain rates from the National Climatic Data Center (NCDC). The differences in the measured and the observed rain rates are expected, since the measurement locations were a few miles apart. Also,

the rain rate estimates obtained from the camera-based gauge are for a short time duration of 10s while rain rates obtained from NCDC are averaged over a period of one hour. Moreover, conventional rain gauges tend to report low rain rates due to splashing and wind effects (Habib et al., 2001).

9. Photorealistic Rendering of Rain Streaks Close to Camera

In most vision tasks, raindrops typically project to streaks a few pixels in width. At this low resolution streaks are thin enough to make the brightness pattern within the streak irrelevant.²⁹ In contrast, when viewed up close raindrops project to large image regions, revealing the complex intensity pattern within the streaks (see top row of Fig. 19). These patterns arise due to the rapid deformation in shape of a falling raindrop, a phenomena often referred to as *oscillations*. Due to the oscillations, the reflection of light by, and the refraction of light through, a falling raindrop produce complex brightness patterns within a single motion-blurred rain streak captured by a camera or observed by a human. The brightness pattern of a rain streak typically includes speckles, multiple smeared highlights and curved brightness contours as shown in the top row of Fig. 19. Moreover their appearance depends strongly on lighting and viewpoint directions.

We have developed a new model for rain streak appearance that captures the complex interactions between the lighting direction, the viewing direction and the oscillating shape of the drop. Our model is built on the raindrop shape oscillation model which we borrow from the literature in the atmospheric sciences. Studies (Tokay and Beard, 1996; Andsager et al., 1999; Kubesh and Beard, 1993) in the field indicate that the oscillations in a raindrop are predominantly confined to two modes: a rotationally-symmetric, oblate-prolate mode and a non-rotationally symmetric, transverse mode. The shape of a falling raindrop is given by a combination of these two

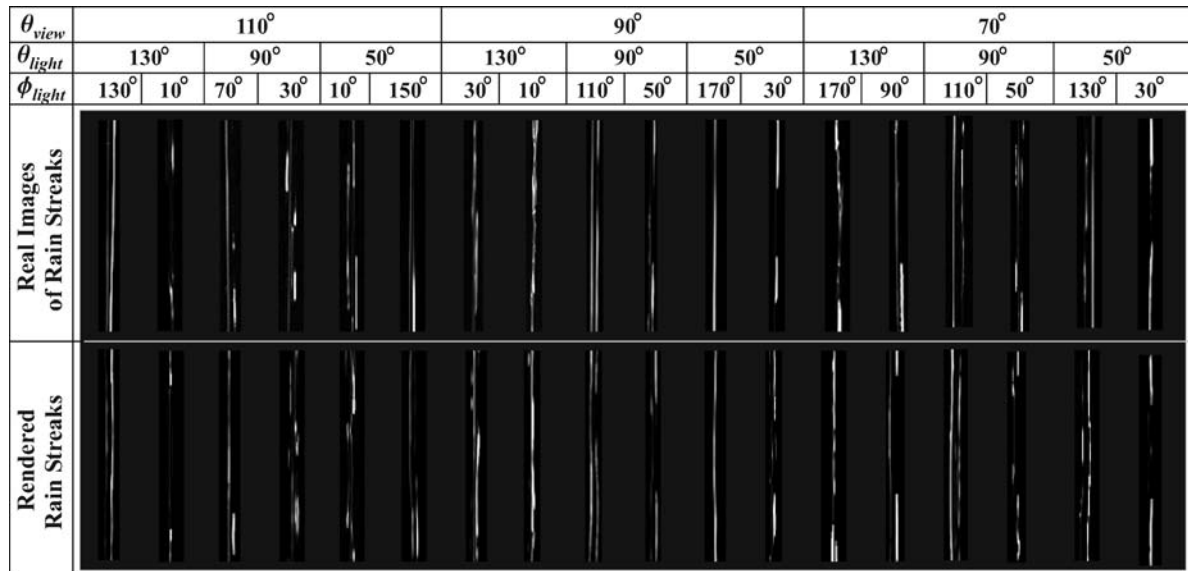


Figure 19. Appearance of actual rain streaks and rendered rain streaks. The top row shows actual images of streaks taken under many different lighting (θ_{light} , ϕ_{light}) and view directions θ_{view} . The complex intensity patterns visible in a rain streak are produced due to the interaction of light with the dynamically changing shape (i.e. oscillations) of the drop. The bottom row shows the rain streaks rendered using our appearance model. The rendered streaks look very similar to the actual rain streaks.

modes. We have empirically verified our streak appearance model by comparing the appearance of rendered streaks with those of actual images of falling rain streaks under a wide range of lighting and viewing conditions. Figure 19 shows a comparison of the rendered and the actual images of streaks at different lighting and view angles. The rendered streaks look very similar to the actual images, thus verifying the accuracy of our model. We have also developed an image-based rain rendering algorithm that uses this streak appearance model to add photo-realistic rain to images and videos. For more details on the appearance model and the rendering algorithm please see (Garg and Nayar, 2006).

10. Conclusion and Future Work

In this work we have shown that analyzing the visual appearance of rain not only improves our understanding of rain but also allows us to develop simple yet effective algorithms for handling rain in vision. This approach has led to two useful algorithms—(a) post-processing algorithm for detection and removal of rain from videos and (b) an algorithm that sets optimal camera parameters to reduce rain visibility during image acquisition. We are currently working on a camera-lens system that automatically detects a rain event (using the post-processing algorithm) and switches to optimal camera parameters for rain reduction.

We would like to extend our work to include the other common dynamic weather condition, snow. How-

ever, snow is much more challenging. The motion of snowflakes depends strongly on wind, making its dynamics difficult to model analytically. Also, various types of snowflakes exist that differ in sizes, shapes and crystal structure. This makes it difficult to develop a general photometric model for snowflakes. Despite these difficulties we believe that as in rain, modeling the key appearance properties of snow will allow us to develop effective algorithms for handling snow in videos.

We have also shown how physics-based modeling of raindrop oscillations allows us to faithfully reproduce complex patterns found in real rain streaks. Other secondary effects such as splashing of raindrops are also important for realistic rendering of rain. We plan to incorporate these effects in our future work.

Dedication to Takeo Kanade

The research presented in this paper was conducted at the Computer Vision Laboratory at Columbia University. This laboratory was established in 1991 by the second author, with physics-based vision as the primary focus of its activities. During all the 15 years of its existence, the activities of the laboratory have been greatly inspired by the research approach and philosophy of Takeo Kanade, who, along with Katsushi Ikeuchi and Steven Shafer, established the first research program devoted to physics-based vision in the mid-1980s at Carnegie Mellon University. Takeo Kanade’s unique approach of first understanding the physical phenomenon underlying a visual process,

modeling it based on its first principles, developing algorithms that exploit the model and experimentally verifying the limits of the algorithm, lies at the core of virtually every project undertaken by the Computer Vision Laboratory at Columbia University. It is an approach that has served as the backbone for the doctoral and post-doctoral research of many individuals, who have gone on to establish their own research programs with similar tenets. We are greatly indebted to Takeo Kanade for imparting his wisdom and values to us.

Appendix

10.1. Photometry of a Raindrop

- (a) *Refraction.* Consider the scene ray \hat{r} in Fig. 20(a). The angle d_r by which the scene ray \hat{r} deflects due to refraction can be calculated by using geometric optics (triangle OAB in Fig. 20(a)) and is given by $d_r = 2(i - q)$. The angle θ_r made by the ray \hat{r} with the z -axis (triangle OCP in Fig. 20(a)) is given by: $\theta_r = d_r - \alpha$, where, α is the angle between \hat{v} and the optical axis of the camera. Substituting value of d_r , q and $i = (\pi - \theta_n + \alpha)$, in the equation for θ_r we get the result in Eq. (7).
- (b) *Internal Reflection.* Consider the scene ray \hat{p} in Fig. 20(a). The angle d_p (not shown in Fig. 20(a)) that the scene ray deflects to reach the observer is obtained by adding the angle of deflection ($i - q$) at point C (refraction), $(\pi - 2q)$ at point A (internal reflection) and $(i - q)$ at exit point B. Hence, $d_p = 2(i - q) + (\pi - 2q)$. It is easy to see that any additional reflection would deflect the ray by an additional angle $(\pi - 2q)$. Hence, for a scene ray that reflects N times from the inside surface of the drop, the angle of deflection is equal to $d_p =$

$2(i - q) + N(\pi - 2q)$. The angle θ_p that the scene ray \hat{p} makes with the optical axis can be written as $\theta_p = d_p - \alpha$. Substituting value of d_p , in the equation for θ_p , we obtain Eq. (12).

- (c) *Radiance of Refracted Light.* In this section, we relate the radiance of the refracted ray to that of the incident ray. Consider a patch of area dA , the flux impinging on this plane from direction \hat{r} (see Fig. 20(a)), $F_r = L_r \cos i \, d\omega_i \, dA$, where, i is the incidence angle, $d\omega_i = \sin(i) \, di \, d\phi$ is the solid angle and L_r is the radiance in the direction \hat{r} . Similarly, the flux dF_A in the direction of the ray refracted at point A (see Fig. 20(a)) is given by $dF_A = L_A \cos q \, d\omega_q \, dA$, where, q is the angle of refraction given by Snell's law and L_A is the radiance of the ray refracted at point A. The amount of the refracted flux is related to the incident flux via Fresnel's coefficient k and is given by $dF_A = (1 - k(i)) \, dF_r$, where, $k(i)$ is the Fresnel's reflectivity coefficient for unpolarized light. Substituting the values of dF_A and dF_r in the above equation we get $L_A = (1 - k(i)) \frac{\cos i}{\cos q} \frac{\sin i \, di}{\sin q \, dq} L_r$. Using Snell's law to relate di and dq the above equation simplifies to $L_A = \mu^2(1 - k(i))L_r$.

10.2. Photometry of Rain Streaks: Motion Blur

Bounds for Photometric Model Parameters. We derive an expression for the time τ that a drop stays over a pixel. Figure 20(b) shows a drop passing through a pixel. Consider the right angled triangle $\triangle ADC$. Then, τ is given by,

$$\tau = \frac{AB + 1}{v_i} = \frac{2\sqrt{a_i^2 - \rho_i^2} + 1}{v_i} < \frac{2a_i + 1}{v_i}, \quad (29)$$

since $0 < \rho_i \leq a_i$. A streak is visible for a drop that projects to a region larger than a pixel i.e. $2a_i > 1$. Then,

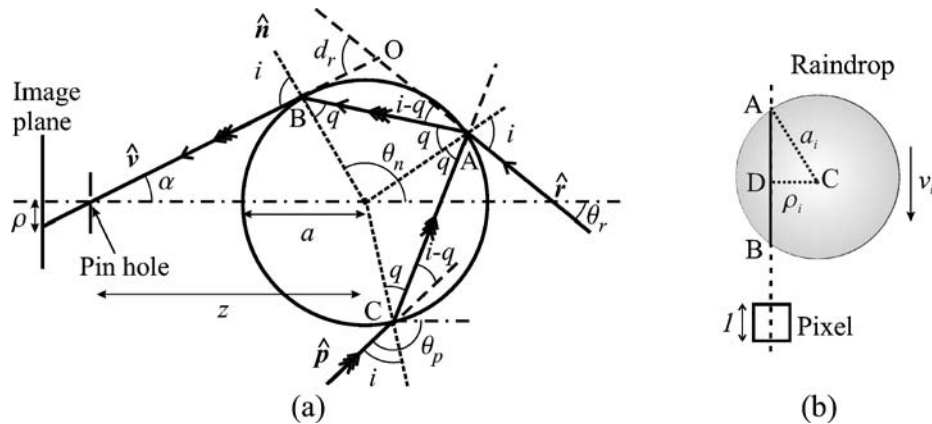


Figure 20. (a) Rays of light from directions \hat{r} and \hat{p} are refracted by the drop towards the camera. The geometric mappings of the rays from scene directions \hat{r} and \hat{p} to the surface normal \hat{n} are unique. (b) Schematic to compute the time τ that a drop stays over a pixel.

we obtain a conservative upper bound $\tau < 4 a_i / v_i$. If f is the effective focal length of the camera and z is the distance of the drop from the camera, then τ can be related to the physical properties of the drop (size a and fall velocity v) by substituting $a_i = \frac{fa}{z}$, and $v_i = \frac{fv}{z}$, to get the range $0 < \tau < 4 a / v$. Substituting v from Eq. (??), we obtain a range of possible values for τ (and hence for $\beta = \tau / T$) in terms of drop size a as $0 < \tau < \sqrt{a} / 50$ sec, $0 < \beta < \sqrt{a} / (50 T)$, where, T is the exposure time, typically 1/30 sec for a video camera. Since the maximum value of $a = 3.5 \times 10^{-3}$ m, the possible ranges for τ and β can be obtained as $0 < \tau < 1.18$ ms and $0 < \beta < 0.039$. Now let us consider the dependence of τ on ρ_i for all pixels within a streak. From Fig. 20(b), we see that ρ_i does not change along the direction of the streak. Further, since the width of the streak (image size of the drop) is only a few pixels, the change in ρ_i across the streak is also negligible. Thus, the dependence of τ on ρ_i is weak and can be neglected. In other words, τ and β are constant for all pixels on a streak.

10.3. Analysis of the Visibility of Rain

- (a) *Raindrop and Exposure Time.* Drops at a distance $z > z_m$ only occlude a fraction $A = \pi (\frac{fa}{z})^2$ of pixel area (in pixels). Also, the time τ a drop stays within the field of view of a pixel is $t = \frac{1}{v_i} \ll T$. To obtain the intensity I_r at a pixel due to a raindrop we integrate the irradiance at the pixel over the exposure time. That is

$$\begin{aligned} I_r &= k \frac{\pi}{4 N^2} \int_0^\tau L(t) dt + \int_\tau^T L(t) dt \\ &= k \frac{\pi}{4 N^2} (\tau A L_r + \tau (1 - A) L_b + (T - \tau) L_b) \end{aligned} \quad (30)$$

Substituting for A , τ , k in terms of k_0 (see Eq. (20)) and subtracting I_b , we get Eq. (22).

- (b) *Variance Due to a Layer of Rain.* Let us look at the intensity fluctuations produced by a thin layer of rain of thickness dz (see Fig. 14). These fluctuations are produced due to a change in the number of drops that a pixel sees over the duration of a frame (i.e. exposure time). The probability $P(k)$ that k number of drops exists in a volume is given by a Poisson distribution (Manning, 1993), that is $P(k) = e^{-\bar{n}} \frac{(\bar{n})^k}{k!}$, where, $\bar{n} = \rho V$ is the mean number of drops in a given volume V and ρ is the density of rain. The volume that a pixel samples during the exposure time is³⁰ $V \approx \frac{z}{f} v T dz$, where v is the velocity of the raindrop and T is the exposure time of the camera. Substituting the value

of V in the expression $\bar{n} = \rho V$, we get

$$\bar{n} = \rho (z/f) v T dz \quad (31)$$

In general, the mean number \bar{n} of drops that a pixel sees is a small fraction. Hence, the chances that two or more drops will affect a pixel during the short exposure time of a camera is very low³¹ and can be neglected. Therefore, the probability P_{drop} that a pixel is affected by a drop is equal to the probability that any pixel within the width of streaks $w^d(z)$ is affected by a drop, i.e. $P_{drop} = P(1) w^d \simeq \bar{n} * w^d$. Hence, the variance due to a thin layer of rain is given by,

$$\begin{aligned} \sigma^2(\Delta I(z)) &= E(\Delta I(z)^2) - E(\Delta I(z))^2 \\ &= P_{drop} \Delta I(z)^2 - P_{drop}^2 \Delta I(z)^2 \end{aligned} \quad (32)$$

Since $P_{drop} \ll 1$, $P_{drop}^2 \ll P_{drop}$, and hence the second term in Eq. (32) can be neglected. Substituting the value of P_{drop} in the above equation we get Eq. (25).

- (c) *Variance Due to a Volume of Rain.* Equation (26) can be written as,

$$\sigma_r^2(I) = k_0^2 \frac{4 a^4 \rho}{v T} (L_r - L_b)^2 \mathcal{G}(f, N, z_0), \quad (33)$$

where, $\mathcal{G}(f, N, z_0) = \int \frac{f dz}{z (w(z) + |b_c(z)|)}$. Since the integral contains $|b_c|$ we get three cases depending on the location of focus plane z_0 .

Case 1: $z_0 > R z_m$

$$\mathcal{G}(f, N, z_0) = \frac{f z_0}{H} \ln \frac{X(z_1)}{X(2fa)} + \frac{f}{1 - \frac{H}{z_0}} \ln \frac{Y(2Rfa)}{Y(2fa)} \quad (34)$$

where, $H = \frac{f^2 p}{F}$, $X(z) = 2fa + H(1 - \frac{z_1}{z_0})$ and $Y(z) = (1 - \frac{H}{z_0})z + H$

Case 2: $z_m < z_0 < R z_m$

$$\begin{aligned} \mathcal{G}(f, N, z_0) &= \left(\frac{f z_0}{H} \ln \frac{X(z_1)}{X(2fa)} + \frac{f}{1 - \frac{H}{z_0}} \ln \frac{z_0}{Y(2fa)} \right. \\ &\quad \left. + \frac{f}{1 + \frac{H}{z_0}} \ln \frac{z_0}{Y'(2fa)} \right)^{\frac{1}{2}} \end{aligned} \quad (35)$$

where, $Y'(z) = (1 + \frac{H}{z_0})z - H$

Case 3: $z_1 < z_0 < z_m$

$$\mathcal{G}(f, N, z_0) = \frac{f z_0}{H} \ln \frac{X(z_1)}{2fa} + \frac{f z_0}{H} \ln \frac{X'(2fa)}{2fa} + \frac{f}{1 + \frac{H}{z_0}} \ln \frac{Y'(2Rfa)}{Y'(2fa)} \quad (36)$$

where, $X'(z) = 2fa - H(1 - \frac{z_1}{z_0})$. Taking the square root of Eq. (33) we get Eq. (27).

Notes

1. In most vision applications raindrops project to a few pixels in width. At this low resolutions the intensity patterns produced due to oscillations are barely visible. Also, in ambient lighting (overcast conditions) the effects of oscillations on streak appearance are weak. These oscillations, however, become important when drops are viewed up-close and illuminated by complex lighting. In such cases, oscillations result in complex intensity patterns within a rain streak as discussed in Section 9.
2. Scattering properties of raindrops have been analyzed (Middleton, 1952; McCartney, 1975; Deepak and Box, 1978), in fields such as atmospheric sciences, signal communication and remote sensing. These fields use active illumination sources such as (lasers) and specialized detectors (photo-cells) to examine rain effects on transmitted signal. However, the appearance of raindrops under natural lighting as seen by a camera is very different from the above studies and has not been done before.
3. Note that radiance is just a variable of surface normal \hat{n} , since the viewing direction \hat{v} depends on \hat{n} .
4. In this case, the image of the drop is not circular but rather elliptical. However, a simple projective mapping relates the elliptical image to its corresponding circular one.
5. Since outdoor illumination (sky, sunlight) is generally unpolarized the Fresnel's reflectivity coefficient k is given by $k = \sqrt{k_{\perp}^2 + k_{\parallel}^2}$.
6. This is obtained from Eq. (8) by substituting $1/\mu$ as the refractive index of air with respect to water and substituting q for i and L_A for $L_e(\hat{r})$.
7. Note that this is a partial internal reflection. It is easy to show from the geometry of a sphere that total internal reflections can never occur in a spherical drop since the maximum angle q_{\max} that a ray inside the drop can make with the surface normal is always less than the critical angle of internal reflection.
8. Specular and internal reflections can also be significant when the environment consists of bright light sources. For example, on a sunny day the specular reflection of sunlight from the drop's surface significantly contributes to the brightness of the drop. In addition, internal reflections can disperse sunlight into its constituent colors, to form a rainbow. Note that since the refractive index depends on the wavelength of light, our appearance model can easily reproduce the visual effects produced by the dispersion of light from raindrops.
9. Since the light source is placed behind the acrylic ball, specular and internal reflections are insignificant (except at edges) and have been ignored.
10. While computing the appearance of the acrylic ball we assumed that the optical axis passes through the center of the sphere and is horizontal. However, in an experimental setup it is extremely hard to align the optical axis in such a way.

11. Raindrops typically stay in 1 or 2 frames. Furthermore, due to motion-blur the brightness of streaks depends on the background intensities. This makes it hard to track raindrops. Also, given that the appearance depends on many factors—the physical properties of rain, the environment and the camera settings—it is difficult to learn a general model of rain appearance.
12. When the background is not stationary over the three frames, we may miss some streaks. However, as discussed later, since we detect rain using a sufficient number of frames, missed rain pixels may be detected in other frames.
13. A linear time sequential labeling algorithm (Matlab function “bwlabel”) (Horn, 1986) is used to segment streaks in the binary video frames.
14. The $(l \times l)$ correlation blocks are noisy and hence gradient methods are not suitable for computing the directions. Instead, we use a set of 17, $(l \times l)$ sized oriented binary masks $(m_0, m_{10}, \dots, m_{170})$, corresponding to the angles $(0^\circ, 10^\circ, \dots, 170^\circ)$. m_0 is created by setting pixels in central and its adjoining row (i.e. $((l+1)/2 - 1, (l+1)/2, (l+1)/2 + 1)$) to one and other pixels to zeros. Other masks are obtained by rotating the horizontally oriented mask m_0 by appropriate angles. Each directional mask is multiplied with correlation blocks to obtain the energy (sum of the resulting image) in that direction. Blocks with high directional correlation have high ratio of maximum to minimum energy. The maximum energy value corresponds to the direction of rain.
15. Typically, the false positive streaks due to camera and object motions vary in direction over time and thus do not exhibit directional correlation.
16. In detecting rain, we did not consider this case in order to minimize false detection due to object/camera motions.
17. (Original images courtesy of New Line Productions-©1999 New Line Productions, Inc.)
18. Raindrops far from a camera project to a size much smaller than a pixel. Thus the intensity at a pixel is due to aggregate scattering (as in fog) from these drops. Hence, the visual effects of distant rain are similar to steady weather (fog).
19. Variance can also occur due to scene motion. Hence, while modeling the visibility of rain a static background is assumed. The analysis of rain visibility itself holds for both static and dynamic scenes.
20. Drops in the region $z > Rz_m$ only produce aggregate scattering effects similar to fog—no dynamic effects are visible.
21. Exact modeling of defocus is required to obtain intensity variations across a rain streak. However, since rain streaks are only a few pixels wide, the intensity variation across a rain streak is not significant and can be neglected.
22. The fact that the projected drops only occupy a portion of the pixel is already taken into account in computing ΔI in Eq. (22).
23. We also compute the noise properties of the camera. For a stationary scene the total variance at a pixel is the sum of rain and camera noise. Since camera noise is independent of rain noise, the variance due to rain can be obtained by subtracting variance due to camera noise.
24. Rain produces directional correlation in videos. Hence, to ensure that variance estimates are from independent pixels we selected 60×30 pixels from a uniform brightness patch that were separated by 5 pixels horizontally and 10 pixels vertically.
25. The selected features are from a region that is visible in the initial and the final frame. Also the KLT parameters were set to the default values predefined in the implementation.
26. The F-number N can be estimated using the depth of field equations that relate the near and far plane to the N and z_0 .
27. For the Canon XL1, when the field of view is 10° Rz_m is approximately 24 m.

28. Defocus primarily affects the width of the streaks. This results in an over-estimated size of raindrops, while velocity estimates are not affected significantly. As a result, defocused drops do not satisfy the size and the velocity relation (Gunn and Kinzer, 1949) given by, $v(a) = 200 \sqrt{a}$. Here, a is the drop's radius and v is its fall velocity.
29. Drops that lie close to the camera are in general severely defocused. Also, in overcast illumination conditions, the intensity variation within the streak is low, hence the patterns are not so visible.
30. The volume of this thin slice of the pyramidal section is approximately equal to $V \approx l_x l_y l_z$, where $l_x = \frac{z}{f}$, $l_y = v T$, and $l_z = dz$ are the lengths of its sides.
31. The ratio $P(2)/P(1) = \bar{n}/2$, which is low as \bar{n} has a very small value.

Acknowledgments

This work was supported in part by an award from the National Science Foundation (IIS-04-12759) and a grant from the Office of Naval Research (N00014-05-1-0188).

References

- Andsager, K., Beard, K.V., and Laird, N.F. 1999. Laboratory measurements of axis ratios for large raindrops. *Journal of the Atmospheric Sciences*, 56:2673–2683.
- Beard, K.V. and Chuang, C.H. 1987. A new model for the equilibrium shape of raindrops. *Journal of Atmospheric Science*, 44(11):1509–1524.
- Birchfield, S. 2005. KLT: An Implementation of the Kanade-Lucas-Tomasi Feature Tracker.
- Borovoy, A.G., Kabanov M.V., and Saveliev, B.A. 1975. Intensity fluctuations of optical radiation in scattering media. *Applied Optics*, 14(11):2731–2739.
- Bradley, S.G., Stow C.D., and Lynch-Blosse, C.A. 2000. Measurements of rainfall properties using long optical path imaging. *American Meteorological Society*, 17:761–772.
- Choi, E. 1995. Numerical modelling of gust effect on wind-driven rain. In *9th International Conference on Wind Engineering*, vol. 9, no. 13, pp. 214–215.
- Chu, T.S. and Hogg, D.C. 1996. Effects of precipitation on propagation at 0.63, 3.5 and 10.6 microns. *Bell System Technical Journal*.
- Cozman, F. and Krotkov, E. 1997. Depth from scattering. *CVPR*, 31:801–806.
- Deepak, A. and Box, M.A. 1978. Forward scattering corrections for optical extinction measurements in aerosol media. 2: Poly-Dispersions. *Applied Optics*, 17:3169–3176.
- Dorsey, J., Pedersen, H., and Hanrahan, P. 1996. Flow and changes in appearance. In *Proceedings of Siggraph*, vo. 79, no. 30.
- Flori, J.P. 1990. Mouillage et Schage D'une Facade Verticale: Analyse Experimentale. *Technical Report EN-CLI 90.2 L, Centre Scientifique et Technique du B, timen*, 1990.
- Garg, K. and Nayar, S.K. 2006. Photorealistic rendering of rain streaks. *ACM Trans. on Graphics (also Proc. of ACM SIGGRAPH)*, 25:996–1002.
- Gunn, R. and Kinzer, G.D. 1949. Terminal velocity for water droplet in stagnant air. *Journal of Meteorology*, 6:243–248.
- Habib, E., Krajewski, W.F., and Kruger, A. 2001. Sampling errors of tipping-bucket rain gauge measurements. *Journal of Hydrology Engineering*, 6:159.
- Horn, B.K.P. 1986. *Robot Vision*. The MIT Press.
- Kubesh, R.J. and Beard, K.V. 1993. Laboratory measurements of spontaneous oscillations of moderate size raindrops. *Journal of the Atmospheric Sciences*, 50:1089–1098.
- Langer, M.S., Zhang, L., Klein, A.W., Bhatia, A., Pereira, J., and Rekhi, D. 2004. A spectral-particle hybrid method for rendering falling snow. In *Rendering Techniques*, pp. 217–226.
- Löffler-Mang, M. and Joss, J. 2000. An optical disdrometer for measuring size and velocity of hydrometeors. *Journal of Atmospheric and Oceanic Technology*, 17:130–139.
- Lomas, A. 2005. The Matrix Revolutions. *Personal Communication*.
- Lucas, B.D. and Kanade, T. 1981. An iterative image registration technique with an application to stereo vision. In *International Joint Conference on Artificial Intelligence*.
- Manning, R.M. 1993. *Stochastic Electromagnetic Image Propagation*. McGraw-Hill, Inc.
- Marshall, J.S. and Palmer, W.M.K. 1948. The distribution of raindrops with sizes. *Journal of Meteorology*, 5:165–166.
- McCartney, E.J. 1975. *Optics of the Atmosphere: Scattering by molecules and particles*. John Wiley and Sons.
- Middleton, W.E.K. 1952. *Vision Through the Atmosphere*. University of Toronto Press.
- Mulvin, L., and Lewis, J. 1994. Architectural detailing, weathering and stone decay. *Building and Environment*, 29(1):113–138.
- Narasimhan, S.G. and Nayar, S.K. 2002. Vision and the Atmosphere. *IJCV*, 48(3):233–254.
- Narasimhan, S.G. and Nayar, S.K. 2003. Contrast restoration of weather degraded images. *IEEE Trans. on PAMI*, 25(6).
- Oakley, J.P. and Satherley, B.L. 1998. Improving image quality in poor visibility conditions using a physical model for degradation. *IEEE Trans. on Image Processing*, 7.
- Website: Submitted rain videos. <http://www.cs.columbia.edu/CAVE/project/>, 2006.
- Michael Reed. 2005. Blue sky studios. *Personal Communication*.
- Schechner, Y.Y., Narasimhan, S.G., and Nayar, S.K. 2001. Instant dehazing of images using polarization. *CVPR*.
- Schonhuber, M., Urban, H.E., Baptista, J.P., Randeu, W.L., and Riedl, W. 1994. Measurements of precipitation characteristics of new disdrometer. In *Proceedings of Atmospheric Physics and Dynamics in the Analysis and Prognosis of Precipitation Fields*.
- Starik, K. and Werman, M. 2003. Simulation of rain in videos. *Texture Workshop, ICCV*.
- Tan, K. and Oakley, J.P. 2000. Enhancement of color images in poor visibility conditions. *ICIP*, 2.
- Tokay, A. and Beard, K.V. 1996. A field study of raindrop oscillations. part I. *Journal of Applied Meteorology*, 35.
- Wang, N. and Wade, B. 2004. Rendering falling rain and snow. *SIGGRAPH (sketches 0186)*.
- Wang, T. and Clifford, S.F. 1975. Use of rainfall-induced optical scintillations to measure path-averaged rain parameters. *Journal of the Optical Society of America*, 8:927–937.